Enhancing air–sea CO_2 exchange and modulating seawater carbonate–pH dynamics: the role of wave effect mechanisms in the POP2–waves coupled model

Yung-Yao Lan[1,2], Huang-Hsiung Hsu[1], Wei-Liang Lee[*1] and Simon Chou[1]

[1]Research Center for Environmental Changes, Academia Sinica, Taipei 11529, Taiwan

[2]National Land Resources Conservation Center, National Chung Hsing University, Taichung 40227, Taiwan

Correspondence to: Wei-Liang Lee (leelupin@gate.sinica.edu.tw)

Abstract

In this study, a wave module is online-coupled into the Parallel Ocean Program version 2 (POP2) within the CESM1.2.2 framework (hereafter POP2–waves). Unlike empirical data analyses of observation-based products and offline-forced ocean models that treat wave-induced gas transfer velocity and the air–sea difference in partial pressure of CO_2 (ΔpCO_2) as decoupled variables, the online-coupled POP2–waves model captures their interactive, ΔpCO_2-mediated negative feedbacks. This setup enables wave properties to dynamically modulate gas transfer velocity and physical mixing through sequential processes. POP2–waves is evaluated alongside a control simulation (B–CTL) against the National Oceanic and Atmospheric Administration (NOAA) CarbonTracker (CT2022) inversion product. The spatial air–sea CO_2 flux in POP2–waves simulation shows generally closer structural agreement with NOAA CT2022 than the control B–CTL, thereby improving performance in most selected regions. Specifically, bubble-mediated transfer accounts for up to 41.3% of the total flux, consistent with the ~40% contribution reported in recent research. Although the inclusion of waves (POP2–waves) enhances regional oceanic CO_2 uptake by 11.8% and outgassing by 41.6%, these two processes largely offset each other. Consequently, this dual enhancement results in only a slight 1.8% increase in the global net ocean CO_2 sink compared to the B–CTL simulation. Globally, air–sea ΔpCO_2 and pH exhibit the strongest positive and negative regression coefficients with the air–sea CO_2 flux,

respectively. Regionally, the gas transfer velocity shows a positive (negative) regression coefficient within oceanic CO_2 outgassing (uptake) regions, whereas SST displays the opposite trend.

1. Introduction

The exchange of CO_2 between the air and sea is a crucial component of the global carbon cycle, carrying significant implications for Earth's climate (Bange et al., 2024; Friedlingstein et al., 2022; McKinley et al., 2020; Müller et al., 2023; Shutler et al., 2019). Traditionally, this air–sea exchange is characterized using the bulk formula (e.g., Wanninkhof, 1992, 2014; McKinley et al., 2020; Dong et al., 2022; Fay et al., 2021; Zhou et al., 2023; Heimdal et al., 2024):

$$F_{\mathrm{CO_2}} = k_{\mathrm{w},660} \cdot k_0 \cdot (p\mathrm{CO_2^w} - p\mathrm{CO_2^a}) \cdot (1 - ice) \quad (1)$$

where the air–sea CO_2 flux ($F_{\mathrm{CO_2}}$, mol m^{-2} yr^{-1}) is determined by the gas transfer velocity expressed relative to a Schmidt number of 660 ($k_{w,660}$, cm hr^{-1}), the difference in partial pressure of CO_2 (ΔpCO_2, μatm) between the seawater and atmosphere (indicated by superscripts " w " and " a ", respectively), and the solubility constant (k_0; mol m^{-3} atm^{-1}), which varies with salinity and temperature (Weiss, 1974). Note that an appropriate scaling factor (8.76×10^{-5}) is implicitly required to convert the dimensions of $k_{w,660}$ and ΔpCO_2 into the final flux unit (mol m^{-2} yr^{-1}). The sign of air–sea CO_2 flux is determined by ΔpCO_2, where a positive air–sea CO_2 flux indicates ocean outgassing to the atmosphere. Additionally, the calculated fluxes are weighted by the ice-free fraction (1 – *ice*), where '*ice*' represents the sea ice fraction. The estimation of bulk air–sea CO_2 fluxes using the gas transfer velocity is typically based on the Wanninkhof (1992) formulation:

$$k_{\mathrm{w},660} = 0.31 \langle U_{10}^2 \rangle (Sc/660)^{-0.5} \quad (2)$$

where $\langle U_{10}^2 \rangle$ represents the squared neutral mean wind speed at 10 m above the surface

(m s^{-1}), and *Sc* denotes the Schmidt number. The flux estimate error can reach as high as 34% due to model limitations and uncertainties surrounding bulk parameters (Signorini and McClain, 2009). Furthermore, substantial uncertainties persist in air–sea CO_2 flux estimates, primarily stemming from an incomplete understanding of the spatiotemporal variability in the governing mechanisms (Shutler et al., 2019).

Some studies have highlighted that estimating air–sea CO_2 fluxes involves complexities well beyond neutral wind speed and solubility factors. Monahan and Spillane (1984) previously regarded whitecaps as "low impedance vents" that effectively "shorten" the water-side transfer resistance. Without wave breaking, air–sea CO_2 exchange occurs via mass transport, which under non-turbulent conditions is governed by molecular diffusion; wave breaking then acts as a transitional process from laminar to turbulent flow (Deike, 2022). Furthermore, bubbles provide additional surface area for gas transfer; as they rise through the aqueous mass boundary layer and burst at the sea surface, they significantly enhance near-surface turbulence (Soloviev and Lukas, 2010; Bell et al., 2017; Deike and Melville, 2018; Krall et al., 2019; Czerski et al., 2022). Gutiérrez-Loza et al. (2022) pointed out that during high and intermediate wind speeds (above 6–8 m s^{-1}), enhanced air–sea CO_2 exchange is primarily driven by wave-breaking dynamics and bubble mediation, which occur alongside the generation of sea spray droplets that contribute to atmospheric cloud condensation nucleation. Conversely, under low wind conditions (below 6 m s^{-1}), water-side convection becomes the dominant control mechanism. Beyond these calm periods, the critical role of breaking waves and bubble injection mechanisms in facilitating CO_2 transfer has been widely corroborated (e.g., Andreas et al., 2016; Brumer et al., 2017; Blomquist et al., 2017; Reichl and Deike, 2020; Li et al., 2023; Zhou et al., 2023; Rustogi et al., 2025). Specifically, Deike and Melville (2018) demonstrated that the bubble-mediated contribution to CO_2 transfer exceeds 40% at a neutral 10-meter wind speed (U_{10}) ≥ 10

m s^{-1}, becomes dominant at $U_{10} \geq 15$ m s^{-1}, and reaches 60% at 20 m s^{-1}.

Monitoring sea surface CO_2 is crucial for understanding Earth system dynamics, as climate change has begun to impact the ocean's carbon uptake capacity (Behncke et al., 2024). However, air–sea CO_2 flux estimates derived from products based on the partial pressure of CO_2 (pCO_2) often suffer from significant uncertainties, stemming primarily from the empirical parameterization of the gas transfer velocity (e.g., Williams et al., 2017; Gray et al., 2018; Coggins et al., 2023; Behncke et al., 2024; Fay et al., 2024; Yang et al., 2024). To resolve this issue and independently constrain $k_{w,660}$, direct flux measurements using the eddy covariance (EC) method are widely utilized as a benchmark (Dong et al., 2021). By directly acquiring the turbulent flux F_{CO_2} via the EC method and pairing it with simultaneous measurements of ΔpCO_2, researchers can inversely calculate the gas transfer velocity ($k_{w,660} = F_{CO_2} / (k_0 \times \Delta pCO_2)$). This approach provides a direct observational constraint to evaluate and calibrate these observation-based products under complex marine conditions. However, obtaining reliable direct fluxes from shipborne EC setups presents its own instrumental challenges. Marine EC measurements are generally conducted using either open- or closed-path infrared gas analyzers. A closed-path analyzer (e.g., LI-7000, LI-COR) operates with an enclosed measurement chamber (Sutton et al., 2014, 2021; Bakker et al., 2016; Sabine et al., 2020; Akhand et al., 2021; Wu and Qi, 2023), whereas open-path analyzers (e.g., LI-7500, LI-COR) measure infrared absorption directly in ambient air (Edson et al., 2011; Tokoro et al., 2014; Bell et al., 2017; Dong et al., 2021; Van Dam et al., 2021). While both configurations are inherently susceptible to H_2O cross-sensitivity, each system possesses distinct advantages and systematic limitations (Honkanen et al., 2018). Evaluating and constraining global Earth system models (ESMs) against direct, long-term observations of air–sea CO_2 flux remains challenging due to the severe scarcity of continuous field measurements. Consequently, alternative

validation datasets are typically derived by upscaling sparse in situ pCO_2 observations through a combination of statistical interpolation, machine learning, atmospheric inversion, and climatological averaging to construct long-term, gridded flux products.

Although several recent studies have estimated the air–sea CO_2 flux using Eq. (1), current parameterizations in oceanic and atmospheric models still rely exclusively on neutral wind speed (Long et al., 2013; Moore et al., 2013; Couldrey et al., 2016; Jin et al., 2017; Lovenduski et al., 2019; Ziehn et al., 2020; Chikamoto and DiNezio, 2021). Similarly, surface ocean observation-based products typically calculate those fluxes using standard parameterizations (Wanninkhof, 1992, 2014; Fay et al., 2021). Importantly, the persistent uptake of anthropogenic CO_2 is lowering seawater pH and altering the carbonate system in nonlinear ways, further reducing the oceans' capacity to absorb additional CO_2 (Moore et al., 2013). The mechanisms by which breaking waves and bubble injection enhance total gas transfer velocity have been investigated primarily through empirical analyses of observation-based products (e.g., Andreas et al., 2016; Blomquist et al., 2017; Reichl and Deike, 2020; Zhou et al., 2023). Rustogi et al. (2025) employed a fully coupled ocean-biogeochemistry modeling system based on the MOM6 ocean circulation model and the COBALTv2 biogeochemical module. Utilizing this framework, they simulated ocean dynamics, temperature, and carbon cycling processes—including dissolved inorganic carbon (DIC) and pCO_2—while explicitly accounting for wave effects on air–sea CO_2 exchange. Furthermore, they identified a nonlinear pCO_2 feedback mechanism within the coupled ocean-carbon system that regulates air–sea CO_2 flux. However, their configuration relies on ocean and biogeochemical modules that are strictly forced by offline atmospheric reanalysis and wave model outputs. This decoupled or unidirectional forcing approach is limited in capturing high-frequency, transient air–sea interactions (e.g., rapid wind shifts or wave breaking dynamics) that significantly modulate gas exchange. In contrast, our

study introduces an online coupling framework that integrates wave effects directly into the flux simulation interface at each model time step. This online approach provides a critical advantage: it enables real-time, interactive feedback between wave dynamics and the seawater carbonate system, thereby capturing the nonlinear high-frequency physical controls on the air–sea CO_2 flux that offline-forced systems typically miss.

In this study, we investigate how breaking waves and bubble injection mechanisms influence air–sea CO_2 flux and the ocean's buffering capacity. Specifically, we examine the biogeochemical responses driven by these physical mechanisms within the seawater carbonate–pH system. To achieve this, we utilize the Parallel Ocean Program version 2 (POP2; Smith et al., 2010) of the Community Earth System Model version 1.2.2 (CESM1.2.2; Hurrell et al., 2013) online-coupled with the wave module (Mellor et al., 2008) of the Princeton Ocean Model (POM; Blumberg and Mellor, 1987). The coupled configuration is referred to as the POP2–waves model.

The structure of this paper is organized as follows. Section 2 introduces the model, data, methodology, and experiments employed in this study, and defines twelve key regions of high air–sea CO_2 flux variability identified by the NOAA CarbonTracker data assimilation system (CT2022; Jacobson et al., 2023) to validate the model simulation. Section 3 evaluates the performance of the POP2–waves coupled model in simulating air–sea CO_2 flux and its interaction with the carbonate–pH system over the Western Pacific (WP; 160–180°E, 35–40°N) and the Equatorial Pacific (EP; 230–250°E, 0–5°S) regions. Section 4 compares the carbonate–pH dynamics of POP2–waves and B–CTL, examines the primary drivers of air–sea CO_2 exchange, and evaluates the uncertainties arising from the absence of a ΔpCO_2-driven negative feedback. Finally, Section 5 presents the conclusions.

2. Data, model experiments, and methodology

2.1 Description of the model framework and experiments

In this study, we investigate the role of waves and bubble mechanisms in modulating the ocean's biogeochemical response by comparing the control simulation (B–CTL) with the coupled POP2–waves model within the CESM1.2.2 framework (Fig. 1). The CESM simulation was conducted using a fully coupled component set over a 30-year period, with well-mixed greenhouse gases (CO_2, CH_4, N_2O, etc.), ozone, and aerosols fixed to year-2000 values (the B_2000_CAM5 compset). The framework features a horizontal resolution of 1.9° × 2.5° for both the Community Atmosphere Model 5.3 (CAM5.3) and the Community Land Model version 4 (CLM4). In contrast, the ocean component (POP2; configured with 60 vertical layers) and the prognostic Los Alamos Sea Ice Model (CICE) share a nominal 1° horizontal resolution. State fields and fluxes are exchanged across these differing grids via the coupler (CPL) (Hurrell et al., 2013). POP2 is forced by CAM5.3 through CPL via four primary fields: (1) momentum fluxes (zonal and meridional wind stress and friction velocity), (2) heat fluxes (net shortwave radiation, sensible heat flux, longwave radiation, and heat flux from snow/ice melt), (3) freshwater fluxes (precipitation, evaporation, river runoff, and ice melt), and (4) surface winds (10 m zonal and meridional wind speeds). Furthermore, POP2 interacts with the Biogeochemical Elemental Cycling (BEC; Moore et al., 2013) module to regulate carbonate chemistry and air–sea CO_2 fluxes. This interaction is mediated via ocean dynamics (currents and sea surface height), the K-profile vertical mixing, and tracer transport, with wave-induced processes providing additional physical constraints. Within the BEC module, variations in DIC and nutrients (NO_3, PO_4, and Fe) are primarily controlled by biological processes: photosynthesis consumes DIC and nutrients, whereas respiration and remineralization return organic carbon to the DIC pool. Together with the wave module, these biogeochemical and physical processes jointly regulate the carbon cycle.

The control simulation (B–CTL), which served as the baseline for air–sea CO_2 flux and seawater acidification, utilized Eq. (1) with the gas transfer velocity parameterization from Wanninkhof (1992) (Eq. 2). Both the B–CTL and POP2–waves experiments were integrated under a present-day scenario (starting from the year 2000) to estimate air–sea CO_2 flux and pH variations. This experimental design allows us to isolate the impact of wave effects on carbonate chemistry and directly compare our results with the NOAA CT2022 data assimilation system. For the POP2–waves experiment, the wave module (Mellor et al., 2008) from the POM was online-coupled with POP2. This configuration incorporated bubble-mediated gas transfer—computed from a mechanistic model for air bubble entrainment at the breaking-wave scale (Deike and Melville, 2018)—and was integrated with the POP2 marine biogeochemistry module.

Specifically, the POP2–waves experiment adopts the advanced parameterization framework expanded by Reichl and Deike (2020), and Deike (2022). In this framework, both the non-bubble and bubble-mediated gas transfer velocity are explicitly resolved as a function of the ocean surface friction velocity (u^*, m s^{-1}) and significant wave height (H_s, m). This parameterization effectively captures the main wave effect, as well as solubility and diffusivity. To standardize the formulation for CO_2, the total gas transfer velocity is expressed relative to a Schmidt number of 660. Following Deike and Melville (2018), it is calculated as the sum of the non-bubble ($k_{\mathrm{wNB},660}$) and bubble ($k_{\mathrm{wB},660}$) components:

$$K_{\mathrm{w},660} = K_{\mathrm{wNB},660} + K_{\mathrm{wB},660} = A_{NB} u^* \left(\frac{Sc}{660}\right)^{-1/2} + \frac{A_B}{K_0 R T_0} (u^*)^{5/3} (g H_S)^{2/3} \left(\frac{Sc}{660}\right)^{-1/2} \quad (3)$$

where A_{NB} is an empirical, nondimensional coefficient set to 1.55×10^{-4}, A_B is a dimensional fitting coefficient (1.2×10^{-5} s^2 m^{-2}), R is the ideal gas constant (0.082 L atm mol^{-1} K^{-1}), T_0 is the sea surface temperature (SST, in K), and g is gravitational

acceleration (9.806 m s^{-2}). Section 3.3 examines the relative contributions of the non-bubble and bubble components in simulating the air–sea CO_2 flux.

The marine carbonic acid system is a nonlinear, coupled system governed by CO_2 dissolution equilibrium, $(CO_{2(aq)} + H_2O \overset{K_H}{\leftrightarrow} H_2CO_{3(aq)})$, where the Henry's constant (K_H) for CO_2 in water at 25°C is approximately 3.4 x 10^{-2} (m atm^{-1}), two-step dissociation reactions, and the conservation of the total dissolved inorganic carbon (DIC) and total alkalinity (TA), ultimately determining pH and the distribution of carbonate species. Carbonic acid (H_2CO_3) has two hydrogen ions and dissociates in two steps:

$$H_2CO_3 \overset{K_{a1}}{\longleftrightarrow} H^+ + HCO_3^- \qquad K_{a1} = 4.4 \times 10^{-7} \tag{4}$$

$$HCO_3^- \overset{K_{a2}}{\longleftrightarrow} H^+ + CO_3^{2-} \qquad K_{a2} = 4.7 \times 10^{-11} \tag{5}$$

The DIC can be expressed as

$$\begin{aligned} \mathrm{DIC} &= [H_2CO_3] + [HCO_3^-] + [CO_3^{2-}] \\ &= K_H pCO_2^w + \frac{K_{a1} K_H pCO_2^w}{[H^+]} + \frac{K_{a1} K_{a2} K_H pCO_2^w}{[H^+]^2} \\ &= K_H pCO_2^w \left(1 + \frac{K_{a1}}{[H^+]} + \frac{K_{a1} K_{a2}}{[H^+]^2}\right) \\ &= K_H pCO_2^w ([H^+]^2 + K_{a1}[H^+] + K_{a1} K_{a2})/[H^+]^2 \end{aligned} \tag{6}$$

The marine carbonate system describes the distribution of DIC among its chemical species in seawater and is jointly governed by TA and pH. From Eq. (6), if the oceanic pCO_2^w and pH are known, the DIC can be determined; conversely, pCO_2^w can be derived from DIC. Following Dickson (1981), TA represents the net proton-neutralizing capacity of weak acid anions in seawater and is expressed as

$TA = [HCO_3^-] + 2[CO_3^{2-}] + [B(OH)_4^-] + [OH^-] + [HPO_4^{2-}] + 2[PO_4^{3-}] + [SiO(OH)_3^-] + [NH_3] + [HS^-] - [H^+] - [H_3PO_4]$. In the POP2–waves framework, TA, DIC and biogeochemical processes are used to calculate pH and pCO_2^w.

When TA increases, seawater becomes more alkaline, leading to a higher CO_3^{2-} concentration and enhanced buffering of hydrogen ions. Consequently, $[H^+]$ decreases, causing pH to rise and boosting the ocean's capacity to absorb CO_2. Conversely, when TA decreases, the buffering capacity weakens, $[H^+]$ increases, and pH drops, rendering the ocean more acidic with a reduced capacity for CO_2 uptake.

2.2 Coupling POP2–waves Methodology

Except for the ocean component, all other components adhere strictly to the CESM 1.2.2 framework. The wave module is forced by variables exchanged through the coupler, POP2, and a dedicated input initialization file. Specifically, in addition to the baseline component interactions in CESM1.2.2, the framework passes the zonal and meridional 10-m winds, along with surface friction velocity (u^*, accounting for both open-ocean and sea-ice fractions) from the CPL to evaluate the wave properties and the associated gas transfer velocity. To drive the wave module calculations, key physical variables are retrieved from POP2; this involves interpolating depth-variable currents from POP2 z-coordinates (60 levels of zonal and meridional horizontal velocities) onto POM (waves) sigma-coordinates (21 vertical levels). This vertical mapping is required to compute both the depth-dependent wave radiation stresses and the specified spectrum. Additionally, spatial grid configurations in the x, y, and z directions, along with time-step settings, are exchanged. The wave module further integrates external variables (F1–F4), which represent the spectrally averaged wave radiation stress components used to force the momentum equation.

Following Mellor et al. (2008), the significant wave height (H_s) used in calculating wave radiation stresses represents the total wave energy integrated over the full spectrum, which inherently encompasses both locally wind-generated seas and remotely generated swells. During the simulation of wave energy and propagation,

improper handling of parallel boundary formulations within the domain decomposition can induce artificial wave energy accumulation at the subdomain interfaces. To address this issue, this study mirrors the parallel computing infrastructure of the POP2 Message Passing Interface (MPI) protocol. Key physical and prognostic variables—including the zonal and meridional 10-m winds, wave radiation stress, subsurface momentum, and wave radiation and energy densities—are explicitly exchanged across processor subdomains to establish a robust, scalable online-coupling framework.

2.3 Model Validation

We evaluate the simulated spatial patterns of the air–sea CO_2 flux from both the uncoupled control simulation (B–CTL) and the coupled POP2–waves simulation against estimates from the NOAA CT2022 data assimilation system. Unlike our forward, ocean-centric modeling frameworks, CT2022 optimizes the system from an atmospheric perspective, utilizing a top-down approach to infer net surface CO_2 fluxes by assimilating observed atmospheric CO_2 mole fractions. Consequently, this product captures the integrated signature of both anthropogenic emissions and natural carbon cycle variability to provide continuous global flux estimates spanning from 2000 to 2020.

Following the inversion framework established by Jacobson et al. (2007), NOAA CT2022 partitions the global ocean into 30 distinct basins to capture large-scale circulation and biogeochemical dynamics. This basin-based approach groups regions characterized by coherence in physical processes—such as major current systems, upwelling zones, and boundary mixing layers—as well as shared biogeochemical characteristics, including air–sea CO_2 exchange rates and biological productivity. Moreover, because numerous observational datasets and ocean carbon products are resolved at regional scales, a basin-scale aggregation ensures greater methodological

consistency. We evaluate the seasonal variability and mean state of global air–sea CO_2 fluxes, specifically excluding regions characterized by seasonal flux sign reversals—a feature that can introduce substantial artifacts during model–data comparisons. Instead, our analysis focuses primarily on regions exhibiting robust, clear oceanic CO_2 flux signals. Recognizing that inherent uncertainties in atmospheric inversions stem from sub-grid-scale anthropogenic emissions and localized sea-ice melt, we follow the protocols of Fay et al. (2024) and exclude both the coastal ocean and high-latitude marginal ice zones from our model–data evaluation.

Based on the spatial patterns of oceanic CO_2 outgassing, uptake, and low-flux regimes characterized in the Pacific (Fig. 2c), this study delineates 12 key regions exhibiting high air–sea CO_2 flux variability as identified by NOAA CT2022 (Fig. 2d). These are selected from the 30 ocean basins defined in the CT2022 model documentation (Jacobson et al., 2023) for optimizing flux inversions. These oceanic domains are categorized into three major basins: (1) the Pacific Ocean, (2) the Indian Ocean, and (3) the Atlantic Ocean (Table 1). Within the Pacific basin, specific labels denote regions exhibiting the most pronounced oceanic CO_2 outgassing (the Equatorial Eastern Pacific, EEP) and uptake (the Northeastern Pacific, NEP).

3. Results

3.1 The climatological mean and seasonal variations of air–sea CO_2 flux

We utilize the traditional air–sea CO_2 flux bulk formula (Eq. 1) in CESM1.2.2 while also incorporating wave- and bubble-mediated effects via a gas transfer velocity parameterized by u^*, SST, and H_s (Eq. 3). A comparison of the climatological means and monthly standard deviations indicates that the spatial distribution of the model-simulated air–sea CO_2 fluxes is broadly consistent with NOAA CT2022, with regional differences generally remaining below 0.5 mol m^{-2} yr^{-1} across most analyzed sub-basins

(Figs. 2a–f). Notably, the Pacific CO_2 outgassing and uptake regions simulated by the POP2–waves experiment show smaller range-normalized relative biases (Table 3) against NOAA CT2022 than the B–CTL baseline across most selected regions. This improvement occurs despite POP2–waves having a higher monthly SD across both the Pacific and Indian Oceans.

To ensure an objective and reproducible classification, the 12 ocean regions were categorized into two distinct groups based on rigid statistical criteria, requiring either seasonal phasing consistency or model–data absolute bias magnitudes relative to the NOAA CT2022 baseline to be met:

1. Seasonal phasing consistency (temporal alignment): Regulated by the Pearson correlation coefficient (r) between the simulated monthly flux cycles and NOAA CT2022. Regions assigned to Fig. 3 exhibit consistent seasonal phasing with significantly positive correlations ($r \geq 0.50$), whereas regions in Fig. 4 display prominent phase mismatches or anti-correlated trends ($r < 0.50$ or statistically non-significant r).
2. Relative magnitudes of model–data biases (amplitude deviancy): Defined as the monthly averaged absolute deviation normalized by the overall peak-to-peak seasonal range (95th minus 5th percentile) of the NOAA CT2022 baseline. A threshold of 25% was applied to further distinguish regions where structural amplitude offsets dominate over temporal phase alignment.

Based on these thresholds, the eight regions in Fig. 3 exhibit coherent seasonal phasing and relatively small monthly model–data biases. In contrast, the four regions in Fig. 4 (including the South Atlantic Ocean with $r = 0.33$) display clear structural discrepancies, such as inverted seasonal trends or weak temporal alignment. Importantly, these temporal phase misalignments tend to amplify the calculated monthly model–data biases, as the model and data fluctuate in opposing directions

throughout the annual cycle. This phase mismatch contributes to larger relative monthly mean biases; specifically, the model–data biases averaged across the four regions in Fig. 4 (33.7% in B–CTL and 32.6% in POP2–waves) are markedly larger than those in the eight regions of Fig. 3 (26.4% in B–CTL and 22.0% in POP2–waves).

In terms of the regional mean values of air–sea CO_2 flux, the POP2–waves simulation generally demonstrates closer structural agreement with NOAA CT2022 compared to the uncoupled B–CTL baseline, showing improvements in seven of the eight analyzed regions (with the exception of the Northwest Pacific (NWP); Fig. 3). Nevertheless, despite this larger mean offset in specific regions such as the NWP, POP2–waves successfully captures the autumn transition of oceanic CO_2 from a sink to a source as depicted in NOAA CT2022—a feature that remains unrepresented in B–CTL. Table 3 presents the range-normalized relative magnitudes of model–data biases across eight selected regions, providing a robust metric to evaluate the simulated seawater carbonate system, pH and flux field performance against the NOAA CT2022 atmospheric inversion baseline. Overall, the wave-coupled framework (POP2–waves) demonstrates a widespread reduction in systematic biases across the majority of the analyzed regions compared to the uncoupled control simulation (B–CTL). Specifically, the regional mean absolute deviation dropped noticeably in major ocean basins, with the most pronounced improvement captured in the Equatorial Eastern Pacific (EEP), where the relative bias was drastically attenuated by 25.0% (from 71.5% in B–CTL down to 46.5% in POP2–waves). Notable bias reductions are also observed in the Northwest Pacific (NWP, down by 4.9%), and South Indian Ocean Region 1 (SIO1, down by 4.1%), confirming that incorporating wave-effect mechanisms successfully rectifies over- or under-estimations in air–sea carbon exchange dynamics. Conversely, the uncoupled baseline (B–CTL) exhibits slightly smaller biases in the Equatorial Atlantic Ocean (EAO) (11.9% vs. 15.0%), suggesting potential localized over-

compensations in wave parameterizations within this sub-basin. Nonetheless, the reduction of relative biases across most other regions indicates that the online-coupled framework generally provides an improved representation of air–sea CO_2 fluxes.

The POP2–waves simulation generally exhibits a higher SD than B–CTL, reflecting an amplified seasonal variability (Figs. 3–4). Although these SD values typically remain below 3 mol m^{-2} yr^{-1}, they peak during boreal winter, driven by intense oceanic CO_2 uptake in high-latitude regions of the Northern Hemisphere, such as the Northwestern and Northeastern Pacific, and the North Atlantic Ocean 1. In contrast, the Southern Hemisphere exhibits pronounced monthly SD along with clear oceanic CO_2 uptake during the austral winter (boreal summer), particularly across regions such as the South Pacific Ocean 1 (SPO1), South Indian Ocean 1 (SIO1), and South Atlantic Ocean (SAO). However, the monthly SD derived from NOAA CT2022 shows notable regional variations. In particular, both models underpredict the magnitude of variability observed in the Northwest Pacific (NWP), Equatorial Eastern Pacific (EEP), and North Atlantic Ocean 1 (NAO1).

Four specific sub-basins—South Atlantic Ocean (SAO), South Pacific Ocean Region 2 (SPO2), South Indian Ocean Region 2 (SIO2), and North Atlantic Ocean Region 2 (NAO2)—exhibit prominent model–data discrepancies when evaluated against NOAA CT2022 (Fig. 4). Notably, these systematic deviations are not attributable to wave-mediated processes or the parameterization of the CO_2 flux bulk formula. Within the NAO2, both the B–CTL and POP2–waves models simulate strong seasonal variations that mirror NAO1, characterized by substantial oceanic CO_2 uptake during the boreal winter; conversely, NOAA CT2022 displays the opposite seasonal trajectory in this sub-basin. A structurally similar mismatch is observed in the mid-latitude South Pacific (SPO2 and SIO2), where the simulated seasonal cycles of both models exhibit close synchronization with their respective low-latitude counterparts

(SPO1 and SIO1) but differ noticeably from the inverse trend captured by the NOAA CT2022 atmospheric inversion framework.

3.2 The relationship between U_{10} and $k_{w,660}$ in two regions with contrasting wind speed regimes

To demonstrate that the sea-state-dependent gas transfer velocity (Deike and Melville, 2018) provides a more suitable estimate of air–sea CO_2 flux than the wind-only formulation (Wanninkhof, 1992) under high-wind conditions (U_{10} > 10 m s^{-1}), we selected the Western Pacific (WP) and the Equatorial Pacific (EP) regions due to their contrasting wind regimes. The WP region experiences a high frequency of high-wind conditions (exceeding 30%), whereas wind speeds in the EP region consistently remain below this threshold. Because both regions exhibit stable and significant oceanic CO_2 outgassing or uptake, they enable a clear comparative analysis of the correlation between $k_{w,660}$ and U_{10} (Figs. 5a, b).

Generally, the B–CTL data shows higher R^2 but lower $k_{w,660}$ values compared to those in POP2–waves across both the WP and EP. The POP2–waves experiment exhibits a slightly lower R^2 than B–CTL due to greater deviations between $k_{w,660}$ and U_{10}, particularly at higher surface wind speeds. This pattern is consistent with the findings of Gutiérrez-Loza et al. (2022) under conditions where H_s > 1.5 m. The relationship between $k_{w,660}$ and U_{10} was evaluated under two scenarios: baseline monthly climatological means (H_s < 1.5 m) and high-resolution daily data filtered for H_s > 1.5 m (enhanced conditions) aggregated into 30-year monthly averages. Notably, both approaches substantially diminish the differences in $k_{w,660}$ at identical U_{10} values.

However, short-term (30 min) observations indicate that gas transfer velocity can be up to twice as high under similar wind speeds when H_s > 1.5 m (Gutiérrez-Loza et al., 2022). Divergence between the models becomes significant when U_{10} exceeds 12

417 m s^{-1} over the WP region (Fig. 5a), whereas over the EP region, the convergence of
418 $k_{w,660}$ estimates is most notable around U_{10} = 9 m s^{-1} (Fig. 5b), suggesting that mid-
419 range wind speeds dominate the EP flux signal.

420 As shown in Fig. 5c, the enhanced WP cases (H_s > 1.5 m) have data available for
421 all months except August and October, during these available months, their $k_{w,660}$ values
422 consistently exceed both the all-data POP2–waves and B–CTL averages. In contrast,
423 the EP region exhibits H_s > 1.5 m data only during the summer months (July to October),
424 where corresponding $k_{w,660}$ values also exceed both all-data POP2–waves and B–CTL
425 averages. The monthly SD indicates no significant differences between the enhanced
426 (H_s > 1.5 m) data and the standard POP2–waves simulations over the WP, with the $k_{w,660}$
427 discrepancies between the two datasets remaining minimal from January to May
428 because the average H_s during this period consistently remains below 1.5 m. However,
429 over the EP, a pronounced discrepancy is observed between the H_s > 1.5 m condition
430 and the all-data POP2–waves average from July to September.

431

432 **3.3 Regression of CO_2 flux against U_{10} under high-wind conditions**

433 The wind-only parameterization of gas transfer velocity tends to underestimate
434 values under high-wind conditions (U_{10} > 10 m s^{-1}) or high significant wave heights
435 (H_s > 1.5 m) (e.g., Gutiérrez-Loza et al., 2022; Zhou et al., 2023). Under these high-
436 wind conditions, the monthly mean air–sea CO_2 fluxes derived from the B–CTL and
437 POP2–waves simulations diverge notably within the Western Pacific region (WP)
438 (Fig. 6), highlighting key discrepancies between the wind-only and wave-modified
439 $k_{w,660}$ formulations. The data were filtered to include only grid points that met this
440 high-wind threshold before being regionally averaged. Because not all months
441 contained grid points satisfying the threshold, a final subset of 154 data points was
442 utilized for the linear regression analysis. These high-wind conditions over the WP

region occur primarily in winter (accounting for 42% of the valid data), when the concurrent low sea surface temperatures further enhance CO_2 solubility. The slopes of the regression equations (–0.77 mol m^{-2} yr^{-1} per m s^{-1} for B–CTL and –1.40 mol m^{-2} yr^{-1} per m s^{-1} for POP2–waves) alongside the mean CO_2 fluxes (Y_{avg}: –6.35 mol m^{-2} yr^{-1} for B–CTL and –6.97 mol m^{-2} yr^{-1} for POP2–waves) both indicate that POP2–waves exhibits a higher sensitivity to wind speed, leading to stronger oceanic CO_2 uptake across the WP domain under elevated wind speeds.

The correlation coefficient (R) of the POP2–waves simulation is higher than that of B–CTL, indicating that the sea-state-dependent $k_{w,660}$ formulation provides a more realistic representation of the CO_2 flux than the wind-only $k_{w,660}$ scheme under high-wind conditions. This finding aligns with the observations of Gutiérrez-Loza et al. (2022) and Zhou et al. (2023). The average air–sea CO_2 flux in B–CTL over the WP region during DJF and JJA is −0.021 and −0.004 mol m^{-2} yr^{-1}, respectively. Meanwhile, POP2–waves exhibits only slight discrepancies relative to B–CTL during these respective seasons, with differences ranging between 0.001 and 0.002 mol m^{-2} yr^{-1} in CO_2 uptake (data not shown). This contrast indicates that under high-wind conditions, the episodic air–sea CO_2 flux is significantly greater than the seasonal baseline averages.

3.4 Analysis of surface fields and $k_{w,660}$ component in POP2–waves and B–CTL

The spatial co-variations of sea level pressure (SLP), U_{10}, and H_s underscore their combined role as key meteorological and wave drivers steering the regional $k_{w,660}$ patterns (Figs. 7a, b). The region with $H_s > 1.5$ m is generally situated where $U_{10} > 8$ m s^{-1} and lies south of the high-SLP region. The spatial patterns of climatological U_{10} and H_s align closely with the findings of Reichl and Deike (2020) (Figs. 7a, b). Furthermore, a dominance of bubble-mediated transfer in the POP2–waves simulation, where the

469 $k_{wB,660}/k_{w,660}$ ratio exceeds 0.5, primarily occurs in regions characterized by $H_s > 1.5$ m
470 (Fig. 7b). However, an elevated H_s does not always correspond to a higher $k_{wB,660}/k_{w,660}$
471 ratio in the POP2–waves simulation; this decoupling is explicitly observed in the North
472 Pacific (Fig. 7b).

473 Deike and Melville (2018) demonstrated that the bubble contribution to CO_2
474 transfer exceeds 40% when the $U_{10} \geq 10$ m s^{-1}. In our POP2–waves simulation, the
475 bubble fraction ($k_{wB,660}/k_{w,660}$) accounts for approximately 38% of total gas transfer
476 velocity, which is slightly higher than the ~30% reported by Reichl and Deike (2020).
477 This discrepancy may be attributed to differences in the A_B scaling coefficients (Eq. 3),
478 which are derived from field data, where gas transfer velocity is estimated from eddy
479 covariance flux measurements (Reichl and Deike, 2020; Brumer et al., 2017).

480 The structural differences in $k_{w,660}$ (POP2–waves − B–CTL) reveal that the most
481 pronounced discrepancies are primarily distributed in regions characterized by
482 elevated H_s, particularly in the Southern and South Indian Oceans (Fig. 7c). Although
483 U_{10} in the Indian Ocean and tropical Pacific is relatively low (<5 m s^{-1}; Fig. 7a), the
484 $k_{w,660}$ values simulated by POP2–waves remain approximately 9 cm hr^{-1} higher than
485 those in B–CTL. In these regions, this wave-driven enhancement of the total gas
486 transfer velocity is predominantly governed by the non-bubble-mediated component
487 ($k_{wNB,660}$; Fig. 7d). Although H_s is also elevated in the Southern Ocean (Fig. 7b), it
488 does not contribute substantially to the $k_{w,660}$ difference between POP2–waves and B–
489 CTL; this is because the high U_{10} in this region (Fig. 7a) already yields high gas
490 transfer velocities through the empirical formulation of Wanninkhof (1992). The
491 spatial patterns of both the B–CTL $k_{w,660}$ and the wave-induced $k_{w,660}$ discrepancies
492 (POP2–waves − B–CTL) closely align with the findings of Reichl and Deike (2020)
493 (Fig. 7c). Overall, the two simulations exhibit consistent geographic distributions,
494 yielding 30-year domain-wide mean gas transfer velocities of 17.0 cm hr^{-1} for B–CTL

and 22.7 cm hr^{-1} for POP2–waves, despite their reliance on distinct input parameters (U_{10} versus u^* and H_s). Aside from the polar regions, the total gas transfer velocity in the POP2–waves coupled model exceeds that in B–CTL, with the most pronounced differences localized in the tropics (Fig. 7c). To elucidate the driving mechanisms behind this global enhancement, it is necessary to quantify whether the non-bubble ($k_{wNB,660}$) or bubble-mediated ($k_{wB,660}$) component dominates the total gas transfer velocity across the different ocean basins. This partitioning demonstrates that bubble-mediated processes dominate ($k_{wB,660} > k_{wNB,660}$) under high-H_s conditions, whereas non-bubble mechanisms prevail ($k_{wB,660} < k_{wNB,660}$) in light-wind zones where $U_{10} < 7$ m s^{-1} (Fig. 7).

3.5 Mean State and model differences in pCO_2^w and surface pH

Integrating wave dynamics induces a pronounced spatial reorganization of both pCO_2^w and ocean surface pH over the 30-year climatological period (Fig. 8). Specifically, the baseline B–CTL simulation shows that high pCO_2^w is concentrated in the equatorial eastern Pacific (EEP), contributing to a larger oceanic CO_2 source (Fig. 8a). In contrast, low pCO_2^w is found in high-latitude regions of the Pacific and Atlantic (e.g., NWP, NEP, NAO1, and NAO2), driving strong oceanic CO_2 uptake (Fig. 8a). Over the study period, the climatological standard deviation of pCO_2^w in B–CTL ranges between 10 and 30 ppm (Fig. 8a).

In the CESM1 framework of the B_2000_CAM5 compsets, atmospheric pCO_2^a is held constant (367 ppm). The pCO_2^w in the Eastern Pacific exceeds 440 ppm, indicating an air–sea ΔpCO_2 greater than 73 ppm in B–CTL (109.8 and 92.7 ppm during DJF and JJA, respectively), whereas the pCO_2^w in the Western Pacific is below 320 ppm, indicating an air–sea ΔpCO_2 lower than −47 ppm (−53.4 and −31.4 ppm during DJF and JJA, respectively). Notably, POP2–waves reduces the high pCO_2^w by more than

10 ppm over the Eastern Equatorial Pacific and increases the low pCO_2^w in other regions (Fig. 8b). Consequently, in the oceanic CO_2 outgassing (uptake) regions, the POP2–waves coupled model decreases (increases) pCO_2^w, thereby reducing the magnitude of the air–sea ΔpCO_2. The climatological SD of the pCO_2^w discrepancy between POP2–waves and B–CTL displays marked spatial variability over the Eastern Equatorial Pacific, whereas changes across other regions remain relatively minor.

The biogeochemical module of POP2 (BEC) updates TA in each grid cell by solving a coupled transport–reaction equation (Moore et al., 2013). The average pH of the ocean is currently around 8.1 in oceanic CO_2 uptake regions (e.g., the Western Pacific) and 8.0 in outgassing regions (e.g., the Equatorial Pacific; Fig. 8c), reflecting slightly alkaline conditions. Within the DIC system, bicarbonate ions (HCO_3^-) are the dominant species because background seawater pH falls strictly between pK_{a1} and pK_{a2}. However, continued uptake of atmospheric CO_2 drives a decline in pH—a process termed ocean acidification. Our study highlights that wave-induced $k_{w,660}$ significantly influences the marine CO_2 system, altering alkalinity, pH, and carbonate speciation. These chemical shifts, in turn, provide a feedback mechanism that modulates the overall dynamics of the air–sea CO_2 flux. Consequently, wave-driven perturbations in $k_{w,660}$ directly alter both ΔpCO_2 and net air–sea CO_2 fluxes within the Earth System Model framework.

Ocean pH and surface ocean pCO_2^w are strongly negatively correlated (Macovei et al., 2021). Consequently, low pH values are observed in the Equatorial Eastern Pacific (Fig. 8c), as a direct result of the elevated DIC and pCO_2^w concentrations characteristic of that region (Fig. 8a). Conversely, elevated pH conditions persist in domains with lower pCO_2^w, a signature most prominent throughout high-latitude waters in both the Pacific and Atlantic Basins. Rustogi et al. (2025) indicate that accelerated equilibration of oceanic pCO_2 in the wind–wave–bubble simulation, driven by

enhanced gas exchange, ultimately reduces the magnitude of the air–sea ΔpCO_2. This pCO_2 feedback is strongest in the extratropics, where it suppresses CO_2 uptake. Our POP2–waves experiment reveals a consistent response, characterized by increases in both oceanic pCO_2 (Fig. 8b) and hydrogen ion concentration ($[H^+]$), which are accompanied by a corresponding decline in pH (Fig. 8d) throughout the extratropical ocean basins. Accounting for wave effects results in simulated pH shifts of approximately +0.01 (−0.01) in oceanic CO_2 outgassing (uptake) regions (Fig. 8d). This suggests that incorporating this mechanism alleviates acidification in the equatorial Pacific, whereas it intensifies ocean acidification in the high-latitude domains of both the Pacific and Atlantic Oceans (Fig. 8d). Rustogi et al. (2025) also showed that the effects of Δk_w (the difference between wave-induced $k_{w,660}$ and $k_{w,660}$ based on U_{10}) and ΔpCO_2 (POP2–waves – B–CTL) partially offset each other. However, because the Δk_w effect is generally 20%–30% stronger, it dominates the counteracting ΔpCO_2 effect, explaining the modest changes observed in both oceanic outgassing and uptake CO_2 fluxes within the wave-effect simulation.

4. Discussion

4.1 Impact of wave-dependent k_w on global air–sea CO_2 flux: a comparison between POP2–waves and standard Earth System Models

Several investigations have parameterized the air–sea CO_2 flux using Eq. (1), yet current $k_{w,660}$ parameterizations within prominent global frameworks still rely exclusively on the neutral 10-m wind speed (U_{10}) as seen in models such as MPI-ESM1.2 (Mauritsen et al., 2019), CESM2 (Danabasoglu et al., 2020), NorESM2 (Seland et al., 2020), UKESM1 (Sellar et al., 2019), MIROC6 (Chikamoto and DiNezio, 2021), CMCC-ESM2 (Lovato et al., 2022), and CanESM5 (Sigmond et al., 2023) (Table 2). Concurrently, pioneering efforts have begun quantifying wave-induced effects on both air–sea CO_2 flux and long-term ocean carbon storage by incorporating

574 coupled wind–wave–bubble gas transfer formulations into ocean general circulation
575 models (OGCMs), such as MOM6–COBALTv2 (Rustogi et al., 2025) and NEMO–
576 PISCES (Wu et al., 2025). Importantly, Wu et al. (2025) emphasize that integrating
577 these wave-mediated boundary layer dynamics into fully coupled Earth System Models
578 is crucial to reducing systemic uncertainties in global carbon cycle projections.

579 Several studies have incorporated wave effects following the parameterization of
580 Deike and Melville (2018), utilizing the Surface Ocean CO_2 Atlas (SOCAT) database
581 (Bakker et al., 2016) to calculate diagnostic air–sea CO_2 fluxes. In these offline
582 configurations, however, the computed air–sea CO_2 flux is treated independently of
583 pCO_2^w dynamics and surface pH evolution, lacking any interactive feedback
584 mechanisms between the atmosphere and the upper-ocean carbonate system.

585 Rustogi et al. (2025) utilized an ocean-biogeochemistry system forced by offline
586 atmospheric reanalysis and wave model outputs. While comprehensive, such an
587 offline-forced setup is limited in its ability to capture high-frequency, episodic, and
588 synchronous interactions between physical wave states and surface water chemistry
589 during rapid weather transitions. In contrast, our study implements an online coupling
590 framework. The key added value of our setup is its capacity to simulate step-by-step
591 interactive feedbacks where wave properties dynamically alter the gas transfer
592 velocity ($k_{w,660}$) and physical mixing in real-time. The coupled behavior of POP2–
593 waves includes ΔpCO_2-driven negative feedbacks, which fundamentally differs from
594 traditional obs-based products that treat wave-induced $k_{w,660}$ and ΔpCO_2 as
595 independent variables when estimating air–sea CO_2 flux (e.g., Reichl and Deike,
596 2020). This online coupling mechanism also contrasts with global ocean models
597 forced offline by atmospheric reanalysis and wave model outputs (e.g., Rustogi et al.,
598 2025), where such interactive feedbacks are often omitted. This approach enables our
599 model to resolve non-linear, high-resolution modulations of air–sea CO_2 exchange

600 during rapid dynamic events—effects that are typically muted in offline
601 configurations.
602
603 **4.2 Impact of air–sea ΔpCO_2, $k_{w,660}$, SST, and pH on air–sea CO_2 flux**
604 To evaluate which driver exerts the most direct control on air–sea CO_2 flux, Fig.
605 9 displays the spatial distributions of the linear regression coefficients (LRCs) derived
606 from univariate (one-on-one) linear regressions between the flux and various
607 standardized variables: air–sea ΔpCO_2 (Fig. 9a), $k_{w,660}$ (Fig. 9b), SST (Fig. 9c), and
608 pH (Fig. 9d). To remove the confounding artifacts of differing physical units and
609 enable a direct comparison on a common scale, both the air–sea CO_2 flux and the
610 independent variables were standardized into anomalies (with a mean of 0 and a
611 standard deviation of 1) prior to the regression analysis. The statistical significance of
612 these regressed relationships was subsequently evaluated using a Student's *t*-test at the
613 95% confidence level. Because each standardized regression was performed
614 individually with a single independent variable, the resulting LRCs are equivalent to
615 Pearson correlation coefficients (*r*), constraining their values strictly between −1 and
616 +1. Here, we do not delve into the intricate chemical and biochemical feedback
617 mechanisms governing carbonate species. Nevertheless, it is worth noting that the
618 collective influence of carbonate composition—specifically TA and dissolved
619 inorganic carbon (DIC)—on pCO_2^w variability has been shown to outweigh that of
620 solubility changes driven by sea surface salinity and SST (e.g., Koseki et al., 2023).
621 Among these drivers, air–sea ΔpCO_2 and air–sea CO_2 flux exhibit the strongest
622 positive LRCs, with coefficients ranging from 0.6 to 0.8 across the global ocean; this
623 underscores the ocean's role as a net CO_2 source or sink depending on the sign of the
624 air–sea ΔpCO_2 gradient. Additionally, wave effects increase the LRCs by
625 approximately 0.1 to 0.2, particularly within regions of intense oceanic CO_2

626 outgassing or uptake. Clear positive (negative) LRCs exist between $k_{w,660}$ and the air–
627 sea CO_2 flux in oceanic CO_2 outgassing (uptake) regions. Furthermore, wave effects
628 reduce the absolute LRCs between $k_{w,660}$ and air–sea CO_2 flux in both oceanic CO_2
629 outgassing (uptake) regions (Fig. 9b). This indicates that once interactions between
630 the modeled CO_2 flux and the ocean carbonate–pH system are considered, the wave-
631 influenced CO_2 flux becomes less correlated with $k_{w,660}$ and more closely linked to
632 air–sea ΔpCO_2. This shift can be attributed to the limitations of wind-only
633 parameterizations; as indicated by Zhou et al. (2023), wind-only formulas tend to
634 underestimate gas transfer velocities when U_{10} exceeds 10 m s^{-1}, where intense wave
635 breaking and high significant wave height substantially boost air–sea gas exchange.
636 Furthermore, Johansson et al. (2022) reported that H_s generally increases with wind
637 speed, but the relationship is strongly modulated by wind direction and regional
638 conditions, leading to spatially variable and nonlinear wind–wave coupling.
639 In contrast to the former, there are clear positive (negative) LRCs between SST
640 and CO_2 flux in oceanic CO_2 uptake (outgassing) regions (Fig. 9c). A negative
641 correlation exists between $k_{w,660}$ and SST, reflecting the latitudinal gradient where
642 colder, high-latitude waters are characterized by more intense sea states and elevated
643 $k_{w,660}$ values. This pattern occurs because lower temperatures at high latitudes increase
644 CO_2 solubility (Séférian et al., 2020), thereby enhancing oceanic uptake. From a
645 thermodynamic perspective, higher SST enhances molecular diffusion while lowering
646 seawater viscosity, thereby reducing the Schmidt number ($Sc = v/D$, defined as the
647 ratio of kinematic viscosity (v) to the molecular diffusion coefficient(D)). Because
648 $k_{w,660}$ is parameterized as a function of $Sc^{-0.5}$, a decrease in Sc theoretically elevates
649 $k_{w,660}$. Separately, Fay et al. (2024) attributed the regional discrepancies and variations
650 in air–sea CO_2 fluxes to a combination of factors, including choices in wind speed
651 products, SST datasets, biological carbon uptake, and the parameterization of gas

652 transfer velocity. Wave effects only slightly reduce the LRCs between SST and the
653 air–sea CO_2 flux—by approximately 0.1—within the tropics, with negligible impacts
654 observed in other regions. The strong negative correlation between ocean pH and
655 pCO_2^w is dictated by the acid dissociation equilibria of the marine carbonate system
656 (Fig. 8a, c), which govern the fundamental relationship between dissolved CO_2 and
657 hydrogen ion concentration (Williams et al., 2017). As seawater pH decreases, the
658 resulting increase in hydrogen ion concentration ($[H^+]$) reacts with carbonate ions
659 (CO_3^{2-}). This consumption of carbonate ions reduces the ocean's buffering capacity
660 for CO_2 uptake, causing seawater pCO_2^w to increase. Because atmospheric pCO_2^a is
661 fixed at 367 ppm in the CESM1.2.2 configuration, this rise in surface ocean pCO_2^w
662 narrows the air–sea partial pressure gradient ΔpCO_2 in uptake regions (where
663 seawater pCO_2^w is below atmospheric levels), thereby suppressing the air–sea CO_2
664 influx. Reflecting this mechanism, pH and air–sea CO_2 flux exhibit strong negative
665 LRCs (less than –0.9) across most of the global ocean, with exceptions confined to the
666 Eastern Equatorial Pacific and along the Arctic margins (Fig. 9d). Wave effects
667 marginally attenuate this relationship in the Eastern Equatorial Pacific (EEP),
668 reducing the LRCs by approximately 0.1.
669
670 **4.3 Uncertainty arising from the absence of interactions between air–sea CO_2 flux**
671 **and the ocean carbonate–pH system**
672 Rustogi et al. (2025) indicate that as surface seawater pCO_2^w equilibrates with
673 changes in DIC and alkalinity, the air–sea ΔpCO_2 gradient is partially attenuated.
674 This induces a negative feedback loop whereby enhanced CO_2 uptake (or outgassing)
675 is systematically damped by chemical re-equilibration within the marine carbonate
676 system, a mechanism that is highly consistent with the findings of this study. To
677 assess the uncertainty in CO_2 flux resulting from the absence of interactions between

678 the flux and the ocean carbonate–pH system (i.e., the decoupling of the ΔpCO_2-
679 driven negative feedback), we performed a series of sensitivity experiments. The air–
680 sea CO_2 flux was reconstructed using the uncoupled ΔpCO_2 fields from the control
681 simulation (B–CTL) and the wave-influenced $k_{w,660}$ parameterization from the
682 coupled wave simulation (POP2–waves). This experimental setup explicitly isolates
683 the statistical mean and standard deviation of the flux under a scenario defined by the
684 "lack of ΔpCO_2-driven negative feedback". Only data showing a statistically
685 significant air–sea CO_2 flux difference (at a 95% confidence level) between "lack of
686 ΔpCO_2-driven negative feedback" scenario and POP2–waves are presented in Fig.
687 10b. Compared to the baseline (Fig. 2b), the CO_2 flux under the "lack of ΔpCO_2-
688 driven negative feedback" scenario is stronger than that in the POP2–waves
689 simulation across both oceanic CO_2 outgassing and uptake regions, accompanied by a
690 larger SD. The most pronounced discrepancies occur in the Pacific basin across both
691 outgassing and uptake zones. However, certain mid-to-high latitude subregions—
692 specifically the Northeastern Pacific (NEP), South Indian Ocean 2 (SIO2), and South
693 Pacific Ocean 2 (SPO2)—do not reach the 95% confidence threshold.
694 Rustogi et al. (2025) demonstrate that while wave-enhanced $k_{w,660}$ accelerates
695 local air–sea CO_2 exchange, it simultaneously attenuates the air–sea ΔpCO_2 gradient.
696 In this study, we conceptualize this process as a manifestation of the ocean's buffering
697 capacity, which encompasses the dynamic coupling between CO_2 flux (estimated via
698 $k_{w,660}$) and the marine carbonate–pH system. Within the coupled POP2–waves
699 framework, incorporating wave effects alleviates surface acidification and reduces
700 air–sea ΔpCO_2 over oceanic CO_2 outgassing regions; conversely, the resulting
701 relatively higher pH levels systematically enhance the ocean's capacity to absorb
702 atmospheric CO_2 within oceanic CO_2 uptake regions in the coupled POP2–waves
703 model. In contrast, the simulation lacking the ΔpCO_2-driven negative feedback—

which artificially omits realistic marine buffering effects—overestimates the air–sea exchange, yielding excess CO_2 outgassing into the atmosphere (>0.4 mol m^{-2} yr^{-1}) over source regions. Concurrently, it amplifies excess CO_2 uptake (<−0.4 mol m^{-2} yr^{-1}) within regions characterized by oceanic CO_2 uptake regions (Fig. 10b) compared to the coupled POP2–waves model.

5 Conclusions

The study advances an Earth System Model (ESM) by developing an online coupling framework (POP2–waves) that incorporates wave effects directly into air–sea CO_2 flux simulations, capturing the ΔpCO_2-driven negative feedback within the marine carbonate–pH system. Diagnostically neglecting this coupling by treating ΔpCO_2 and wave-induced $k_{w,660}$ independently leads to a positive bias in global flux calculations, whereas our online coupled simulation captures a buffering negative feedback that moderates the global net response. Fully integrating these wave effects addresses three core modeling challenges:

1. Technical implementation: Resolving grid interpolation, boundary discontinuities in wave energy, and parallel computation.
2. Interdisciplinary analysis: Harmonizing kinematic, thermodynamic, and biogeochemical frameworks across system components.
3. Validation constraints: Overcoming data sparsity by synthesizing indirect flux estimates from atmospheric inversions (e.g., NOAA CT2022), ships, and buoys.

Within the coupled POP2–waves framework, the gas transfer velocity is resolved using the parameterization of Deike and Melville (2018), which attributes bubble-mediated transfer to the combined effects of friction velocity and significant wave height. This setup extends the framework of Wu et al. (2025) by utilizing a dynamically coupled ocean–wave system. This coupling configuration accounts for

how flux-driven alterations in surface ΔpCO_2 feedback to influence the global air–sea CO_2 flux. Our regional evaluation reveals a mixed and basin-dependent performance when introducing wave effects. Across the majority of the 12 key regions of high variability defined by NOAA CT2022, the POP2–waves simulation shows generally closer structural agreement with the inversion data compared to the uncoupled B–CTL baseline. However, this improvement is not universal; notable discrepancies persist within specific sectors, including the Equatorial Atlantic Ocean (EAO), South Pacific Ocean 2 (SPO2), and South Indian Ocean 2 (SIO2), where the wave-coupled model does not clearly outperform the baseline.

Significant deviations between POP2–waves and B–CTL simulations emerge when significant wave height exceeds 1.5 m. Consistent with Gutiérrez-Loza et al. (2022), this wave-induced divergence results in a systematically enhanced air–sea CO_2 flux under high 10-m wind speeds and elevated wave height. Across the entire spatiotemporal domain, the bubble-mediated contribution to the total gas transfer velocity ($k_{wB,660}/k_{w,660}$) in POP2–waves averages approximately 38%. This finding slightly exceeds the ~30% baseline reported by Reichl and Deike (2020). As expected, such elevated ratios are most prominent in these high-wind, rough-sea regions. Concurrently, our results indicate that bubble-mediated processes account for up to 41.3% of the total air–sea CO_2 flux, which is consistent with the ~40% contribution reported by both Reichl and Deike (2020) and Zhou et al. (2023).

Within oceanic CO_2 outgassing regions, POP2–waves attenuates the large air–sea ΔpCO_2 gradient, whereas it slightly amplifies lower gradients elsewhere. This feedback drives surface pH shifts of approximately ±0.01 that spatially correspond to the sign of regional flux. On a global scale, the air–sea ΔpCO_2 (pH) displays the strongest positive (negative) regression coefficients with the flux. Additionally, while

gas transfer velocity scales positively with the absolute air–sea CO_2 flux magnitude, SST demonstrates an inverse relationship with this sensitivity.

Compared to the B–CTL baseline, POP2–waves simulations show that oceanic CO_2 uptake and outgassing regions expand by 11.8% and 41.6%, respectively; however, these two processes largely offset each other, leading to a simulated slight 1.8% increase in the global ocean CO_2 sink. Consequently, while wave-induced enhancements in $k_{w,660}$ boost instantaneous air–sea CO_2 flux, the coupled carbonate–pH system limits the net long-term impact via this ΔpCO_2-driven feedback (Rustogi et al., 2025). This feedback effectively dampens the scaling of local CO_2 flux increases into proportional changes within the global mean ocean carbon sink.

The impacts of the $k_{w,660}$ bulk formula (Wanninkhof, 1992) and wave dynamics (Deike and Melville, 2018) on air–sea CO_2 flux, surface pH, and air–sea ΔpCO_2 are schematically summarized in Fig. 11. The B–CTL baseline captures a pronounced seasonal contrast in Western Pacific air–sea CO_2 fluxes, characterized by strong uptake during DJF that is heavily suppressed in JJA due to SST-driven reductions in solubility. This seasonal variability in air–sea ΔpCO_2 engages a negative feedback loop within the POP2–waves framework, thereby modulating regional flux magnitudes. Conversely, the Equatorial Pacific region exhibits lower pH than the Western Pacific and acts as a persistent CO_2 source across both seasons, showing no obvious seasonal variations—a pattern consistent with Fay et al. (2024).

While the current POP2–waves framework highlights the importance of online coupling and ΔpCO_2-driven feedbacks, several avenues remain to future refine the model. A key priority is the continuous improvement of gas transfer velocity formulations. Future efforts will focus on transitioning to the new generalized formulation proposed by Deike et al. (2025), which incorporates updated coefficients and accounts for an asymmetric bubble flux contribution. While this advancement is

781 expected to have a minor impact on oceanic CO_2 flux estimations, it holds potential
782 significance for constraining global marine O_2 fluxes. Furthermore, moving toward a
783 fully coupled Earth System Model (ESM)—which integrates dynamic atmospheric
784 feedback alongside ocean and wave components—will be pivotal to better unravel the
785 long-term impacts of wave-induced processes on global marine biogeochemical
786 cycles.
787
788 *Code and data availability.* The model code of POP2–waves coupled model is available
789 at https://doi.org/10.5281/zenodo.15795234 (Lan, 2025). Input data of POP2–waves
790 using the climatological Hadley Centre Sea Ice and Sea Surface Temperature dataset,
791 including 30-year numerical experiments, are available at
792 https://doi.org/10.5281/zenodo.5510795 (Lan et al., 2021). CarbonTracker CT2022
793 data are provided by the National Oceanic and Atmospheric Administration (NOAA)
794 and available from Global Monitoring Laboratory
795 https://gml.noaa.gov/aftp/products/carbontracker/co2/CT2022/ (Jacobson et al., 2023).
796
797 *Author contributions.* YYL is the sole developer of the POP2–waves coupled model
798 and writes the majority part of the paper. HHH provides computational support and
799 analysis suggestions. WLL supports reorganization and offers analytical
800 recommendations and SC offers a non-parallel wave module as part of the POM source
801 code.
802
803 *Competing interests*. The authors declare that they have no conflict of interest.
804
805 *Acknowledgements.* Our deepest gratitude goes to the editors and anonymous reviewers
806 for their careful work and thoughtful suggestions that have helped improve this paper

substantially. We would like to thank NOAA GML (Boulder, Colorado, USA) for providing the CarbonTracker CT2022 data from the website at http://carbontracker.noaa.gov (last access: 20 May 2026). We sincerely thank the National Center for Atmospheric Research (NCAR) and their Atmosphere Model Working Group (AMWG) for releasing CESM1.2.2. We are also grateful to the National Center for High- performance Computing, Taiwan for providing the facilities for the computational procedures for running POP2–waves simulations. Thanks, Gemini and ChatGPT for correcting the English grammar.

Financial support. This research received funding from the Taiwan National Science and Technology Council under Grants NSTC 112-2111-M-001-008 and MOST 111-2123-M-001-007, as well as support from the Academia Sinica Grand Challenge Program in Taiwan under Grant AS-GCP-112-M03.

Reference

Akhand, A., Chanda, A., Watanabe, K., Das, S., Tokoro, T., Hazra, S., and Kuwae, T.: Reduction in riverine freshwater supply changes inorganic and organic carbon dynamics and air-water CO_2 fluxes in a tropical mangrove dominated estuary, J. Geophys. Res. G: Biogeosciences, 126, e2020JG006144, https://doi.org/10.1029/2020JG006144, 2021.

Andreas, E., Vlahos, P., and Monahan, E.: The potential role of sea spray droplets in facilitating air–sea gas transfer, in: IOP conference series: earth and environmental science, Vol. 35, p. 012003, IOP Publishing, https://doi.org/10.1088/1755-1315/35/1/012003, 2016.

Bakker, D. C. E., Pfeil, B., Landa, C. S., Metzl, N., O'Brien, K. M., Olsen, A., Smith, K., Cosca, C., Harasawa, S., Jones, S. D., Nakaoka, S., Nojiri, Y., Schuster, U., Steinhoff, T., Sweeney, C., Takahashi, T., Tilbrook, B., Wada, C., Wanninkhof, R., Alin, S. R., Balestrini, C. F., Barbero, L., Bates, N. R., Bianchi, A. A., Bonou, F., Boutin, J., Bozec, Y., Burger, E. F., Cai, W.-J., Castle, R. D., Chen, L., Chierici, M., Currie, K., Evans, W., Featherstone, C., Feely, R. A., Fransson, A., Goyet, C., Greenwood, N., Gregor, L., Hankin, S., Hardman-Mountford, N. J., Harlay, J., Hauck, J., Hoppema, M., Humphreys, M. P., Hunt, C. W., Huss, B., Ibánhez, J. S. P.,

Johannessen, T., Keeling, R., Kitidis, V., Körtzinger, A., Kozyr, A., Krasakopoulou, E., Kuwata, A., Landschützer, P., Lauvset, S. K., Lefèvre, N., Lo Monaco, C., Manke, A., Mathis, J. T., Merlivat, L., Millero, F. J., Monteiro, P. M. S., Munro, D. R., Murata, A., Newberger, T., Omar, A. M., Ono, T., Paterson, K., Pearce, D., Pierrot, D., Robbins, L. L., Saito, S., Salisbury, J., Schlitzer, R., Schneider, B., Schweitzer, R., Sieger, R., Skjelvan, I., Sullivan, K. F., Sutherland, S. C., Sutton, A. J., Tadokoro, K., Telszewski, M., Tuma, M., van Heuven, S. M. A. C., Vandemark, D., Ward, B., Watson, A. J., and Xu, S.: A multi-decade record of high-quality fCO_2 data in version 3 of the Surface Ocean CO_2 Atlas (SOCAT), Earth Syst. Sci. Data, 8, 383–413, https://doi.org/10.5194/essd-8-383-2016, 2016.

Bange, H. W., Mongwe, P., Shutler, J. D., Arévalo-Martínez, D. L., Bianchi, D., Lauvset, S. K., Liu, C., Löscher, C. R., Martins, H., Rosentreter, J. A., Schmale, O., Steinhoff, T., Upstill-Goddard, R. C., Wanninkhof, R., Wilson, S. T., and Xie, H.: Advances in understanding of air–sea exchange and cycling of greenhouse gases in the upper ocean, Elem Sci Anth, 12 (1), https://doi.org/10.1525/elementa.2023.00044, 2024.

Behncke, J., Landschützer, P., and Tanhua, T.: A detectable change in the air–sea CO_2 flux estimate from sailboat measurements, Sci. Rep., 14, 3345, https://doi.org/10.1038/s41598-024-53159-0, 2024.

Bell, T. G., Landwehr, S., Miller, S. D., de Bruyn, W. J., Callaghan, A. H., Scanlon, B., Ward, B., Yang, M., and Saltzman, E. S.: Estimation of bubble-mediated air–sea gas exchange from concurrent DMS and CO_2 transfer velocities at intermediate–high wind speeds, Atmos. Chem. Phys., 17, 9019–9033, https://doi.org/10.5194/acp-17-9019-2017, 2017.

Blomquist, B. W,, Brumer, S. E., Fairall, C. W., Huebert, B. J., Zappa, C. J., Brooks, I. M., Yang, M., Bariteau, L., Prytherch, J., Hare, J. E., Czerski, H., Matei, A., and Pascal, R. W.: Wind speed and sea state dependencies of air–sea gas transfer: Results from the High Wind speed Gas exchange Study (HiWinGS), J. Geophys. Res.-Ocean., 122, 8034–8062, https://doi.org/10.1002/2017JC013181, 2017.

Blumberg, A. F., and Mellor, G. L.: A Description of a Three-Dimensional Coastal Ocean Circulation Model, Costal and Estuarine Science, vol. 4, American Geophysical Union, https://doi.org/10.1029/CO004p0001, 1987.

Boucher, O., Servonnat, J., Albright, A. L., Aumont, O., Balkanski, Y., Bastrikov, V., Bekki, S., Bonnet, R., Bony, S., Bopp, L., Braconnot, P., Brockmann, P., Cadule, P., Caubel, A., Cheruy, F., Codron, F., Cozic, A., Cugnet, D., D'Andrea, F., Davini, P., de Lavergne, C., Denvil, S., Deshayes, J., Devilliers, M., Ducharne, A., Dufresne, J.-L., Dupont, E., Éthé, C., Fairhead, L., Falletti, L., Flavoni, S.,

Foujols, M.-A., Gardoll, S., Gastineau, G., Ghattas, J., Grandpeix, J.-Y., Guenet, B., Guez, Lionel, E., Guilyardi, E., Guimberteau, M., Hauglustaine, D., Hourdin, F., Idelkadi, A., Joussaume, S., Kageyama, M., Khodri, M., Krinner, G., Lebas, N., Levavasseur, G., Lévy, C., Li, L., Lott, F., Lurton, T., Luyssaert, S., Madec, G., Madeleine, J.-B., Maignan, F., Marchand, M., Marti, O., Mellul, L., Meurdesoif, Y., Mignot, J., Musat, I., Ottlé, C., Peylin, P., Planton, Y., Polcher, J., Rio, C., Rochetin, N., Rousset, C., Sepulchre, P., Sima, A., Swingedouw, D., Thiéblemont, R., Traore, A. K., Vancoppenolle, M., Vial, J., Vialard, J., Viovy, N., and Vuichard, N.: Presentation and Evaluation of the IPSL-CM6A-LR Climate Model, J. Adv. Model. Earth Sy., 12, e2019MS002010, https://doi.org/10.1029/2019MS002010, 2020.

Brumer, S. E., Zappa, C. J., Blomquist, B. W., Fairall, C. W., Cifuentes-Lorenzen, A., Edson, J. B., Brooks, I. M., and Huebert, B. J.: Wave-related Reynolds number parameterizations of CO_2 and DMS transfer velocities, Geophys. Res. Lett., 44, 9865–9875, https://doi.org/10.1002/2017GL074979, 2017.

Chikamoto, M. O., and DiNezio, P.: Multi-century changes in the ocean carbon cycle controlled by the tropical oceans and the Southern Ocean, Global Biogeochem. Cy., 35, e2021GB007090, https://doi.org/10.1029/2021GB007090, 2021.

Chikamoto, M. O., DiNezio, P., and Lovenduski, N.: Long-term slowdown of ocean carbon uptake by alkalinity dynamics, Geophys. Res. Lett., 50, e2022GL101954, https://doi.org/10.1029/2022GL101954, 2023.

Coggins, A., Watson, A. J., Schuster, U., Mackay, N., King, B., McDonagh, E., and Poulton, A. J.: Surface ocean carbon budget in the 2017 South Georgia diatom bloom: Observations and validation of profiling biogeochemical argo floats, Deep-Sea Res. II: Top. Stud. Oceanogr., 209, 105275. https://doi.org/10.1016/j.dsr2.2023.105275, 2023.

Couldrey, M. P., Oliver, K. I. C., Yool, A., Halloran, P. R., and Achterberg, E. P.: On which timescales do gastransfer velocities control NorthAtlantic CO_2 flux variability?, Global Biogeochem. Cy., 30,787–802, https://doi.org/10.1002/2015GB005267, 2016.

Czerski, H., Brooks, I. M., Gunn, S., Pascal, R., Matei, A., and Blomquist, B.: Ocean bubbles under high wind conditions – Part 2: Bubble size distributions and implications for models of bubble dynamics, Ocean Sci., 18, 587–608, https://doi.org/10.5194/os-18-587-2022, 2022.

Danabasoglu, G., Lamarque, J.-F., Bacmeister, J., Bailey, D. A., DuVivier, A. K., Edwards, J., Emmons, L. K., Fasullo, J., Garcia, R., Gettelman, A., Hannay, C., Holland, M. M., Large, W. G., Lauritzen, P. H., Lawrence, D. M., Lenaerts, J. T. M., Lindsay, K.,

Lipscomb, W. H., Mills, M. J., Neale, R., Oleson, K. W., Otto-Bliesner, B., Phillips, A. S., Sacks, W., Tilmes, S., van Kampenhout, L., Vertenstein, M., Bertini, A., Dennis, J., Deser, C., Fischer, C., Fox-Kemper, B., Kay, J. E., Kinnison, D., Kushner, P. J., Larson, V. E., Long, M. C., Mickelson, S., Moore, J. K., Nienhouse, E., Polvani, L., Rasch, P. J., and Strand, W. G.: The Community Earth System Model Version 2 (CESM2), J. Adv. Model. Earth Sy., 12, e2019MS001916, https://doi.org/10.1029/2019MS001916, 2020.

Deike, L., and Melville, W. K.: Gas transfer by breaking waves, Geophys. Res. Lett., 45, 10,482–10,492. https://doi.org/10.1029/2018GL078758, 2018.

Deike, L.: Mass transfer at the ocean-atmosphere interface: The role of wave breaking, droplets, and bubbles, Annu. Rev. Fluid Mech, 54, 191–224, https://doi.org/10.1146/annurev-fluid-030121-014132, 2022.

Deike, L., Zhou, X., Rustogi, P., Stanley, R. H. R., Reichl, B. G., Bushinsky, S. M., and Resplandy, L.: A universal wind–wave–bubble formulation for air–sea gas exchange and its impact on oxygen fluxes, Proc. Natl. Acad. Sci. U.S.A., 122, e2419319122, https://doi.org/10.1073/pnas.2419319122, 2025.

Dickson, A. G.: An exact definition of total alkalinity and a procedure for the estimation of alkalinity and total inorganic carbon from titration data, Deep-Sea Res., 28A (6), 609-623, https://doi.org/10.1016/0198-0149(81)90121-7, 1981.

Dong, Y., Yang, M., Bakker, D. C. E., Kitidis, V., and Bell, T. G.: Uncertainties in eddy covariance air–sea CO_2 flux measurements and implications for gas transfer velocity parameterisations, Atmos. Chem. Phys., 21, 8089–8110, https://doi.org/10.5194/acp-21-8089-2021, 2021.

Dong, Y., Bakker, D. C. E., Bell, T. G., Huang, B., Landschützer, P., Liss, P. S., and Yang, M.: Update on the temperature corrections of global air–sea CO_2 flux estimates, Global Biogeochem. Cy., 36, e2022GB007360, https://doi.org/10.1029/2022GB007360, 2022.

Edson, J. B., Fairall, C. W., Bariteau, L., Zappa, C. J., Cifuentes-Lorenzen, A., McGillis, W. R., Pezoa, S., Hare, J. E., and Helmig, D.: Direct covariance measurement of CO_2 gas transfer velocity during the 2008 Southern Ocean Gas Exchange Experiment: Wind speed dependency, J. Geophys. Res., 116, https://doi.org/10.1029/2011jc007022, 2011.

Fay, A. R., Gregor, L., Landschützer, P., McKinley, G. A., Gruber, N., Gehlen, M., Iida, Y., Laruelle, G. G., Rödenbeck, C., Roobaert, A., and Zeng, J.: SeaFlux: harmonization of air–sea CO_2 fluxes from surface pCO_2 data products using a standardized approach, Earth Syst. Sci. Data, 13, 4693–4710, https://doi.org/10.5194/essd-13-4693-2021, 2021.

978 Fay, A. R., Munro, D. R., McKinley, G. A., Pierrot, D., Sutherland, S.
979 C., Sweeney, C., and Wanninkhof, R.: Updated climatological mean
980 ΔfCO_2 and net sea–air CO_2 flux over the global open ocean regions,
981 Earth Syst. Sci. Data, 16, 2123–2139, https://doi.org/10.5194/essd-
982 16-2123-2024, 2024.

983 Friedlingstein, P., Jones, M. W., O'Sullivan, M., Andrew, R. M., Bakker,
984 D. C. E., Hauck, J., Le Quéré, C., Peters, G. P., Peters, W., Pongratz,
985 J., Sitch, S., Canadell, J. G., Ciais, P., Jackson, R. B., Alin, S. R.,
986 Anthoni, P., Bates, N. R., Becker, M., Bellouin, N., Bopp, L., Chau,
987 T. T. T., Chevallier, F., Chini, L. P., Cronin, M., Currie, K. I.,
988 Decharme, B., Djeutchouang, L. M., Dou, X., Evans, W., Feely, R.
989 A., Feng, L., Gasser, T., Gilfillan, D., Gkritzalis, T., Grassi, G.,
990 Gregor, L., Gruber, N., Gürses, Ö., Harris, I., Houghton, R. A., Hurtt,
991 G. C., Iida, Y., Ilyina, T., Luijkx, I. T., Jain, A., Jones, S. D., Kato,
992 E., Kennedy, D., Klein Goldewijk, K., Knauer, J., Korsbakken, J. I.,
993 Körtzinger, A., Landschützer, P., Lauvset, S. K., Lefèvre, N.,
994 Lienert, S., Liu, J., Marland, G., McGuire, P. C., Melton, J. R.,
995 Munro, D. R., Nabel, J. E. M. S., Nakaoka, S.-I., Niwa, Y., Ono, T.,
996 Pierrot, D., Poulter, B., Rehder, G., Resplandy, L., Robertson, E.,
997 Rödenbeck, C., Rosan, T. M., Schwinger, J., Schwingshackl, C.,
998 Séférian, R., Sutton, A. J., Sweeney, C., Tanhua, T., Tans, P. P.,
999 Tian, H., Tilbrook, B., Tubiello, F., van der Werf, G. R., Vuichard,
1000 N., Wada, C., Wanninkhof, R., Watson, A. J., Willis, D., Wiltshire,
1001 A. J., Yuan, W., Yue, C., Yue, X., Zaehle, S., and Zeng, J.: Global
1002 Carbon Budget 2021, Earth Syst. Sci. Data, 14, 1917–2005,
1003 https://doi.org/10.5194/essd-14-1917-2022, 2022.

1004 Gray, A. R., Johnson, K. S., Bushinsky, S. M., Riser, S. C., Russell, J.
1005 L., Talley, L. D., Wanninkhof, R., Williams, N. L., and Sarmiento,
1006 J. L.: Autonomous biogeochemical floats detect significant carbon
1007 dioxide outgassing in the high-latitude Southern Ocean, Geophys.
1008 Res. Lett., 45(17), 9049–9057,
1009 https://doi.org/10.1029/2018GL078013, 2018.

1010 Gutiérrez-Loza, L., Nilsson, E., Wallin, M. B., Sahlée, E., and
1011 Rutgersson, A.: On physical mechanisms enhancing air–sea CO_2
1012 exchange, Biogeosciences, 19, 5645–5665,
1013 https://doi.org/10.5194/bg-19-5645-2022, 2022.

1014 Hajima, T., Watanabe, M., Yamamoto, A., Tatebe, H., Noguchi, M. A.,
1015 Abe, M., Ohgaito, R., Ito, A., Yamazaki, D., Okajima, H., Ito, A.,
1016 Takata, K., Ogochi, K., Watanabe, S., and Kawamiya, M.:
1017 Development of the MIROC-ES2L Earth system model and the
1018 evaluation of biogeochemical processes and feedbacks, Geosci.
1019 Model Dev., 13, 2197–2244, https://doi.org/10.5194/gmd-13-2197-
1020 2020, 2020.

1021 Heimdal, T. H., McKinley, G. A., Sutton, A. J., Fay, A. R., and Gloege,
1022 L.: Assessing improvements in global ocean pCO_2 machine learning
1023 reconstructions with Southern Ocean autonomous sampling,
1024 Biogeosciences, 21, 2159–2176, https://doi.org/10.5194/bg-21-

2159-2024, 2024.

Honkanen, M., Tuovinen, J.-P., Laurila, T., Mäkelä, T., Hatakka, J., Kielosto, S., and Laakso, L.: Measuring turbulent CO_2 fluxes with a closed-path gas analyzer in a marine environment, Atmos. Meas. Tech., 11, 5335–5350, https://doi.org/10.5194/amt-11-5335-2018, 2018.

Hurrell, J. W., Holland, M. M., Gent, P. R., Ghan, S., Kay, J. E., Kushner, P. J., Lamarque, J.-F., Large, W. G., Lawrence, D., Lindsay, K., Lipscomb, W. H., Long, M. C., Mahowald, N., Marsh, D. R., Neale, R. B., Rasch, P., Vavrus, S., Vertenstein, M., Bader, D., Collins, W. D., Hack, J. J., Kiehl, J., and Marshall, S.: The Community Earth System Model: A framework for collaborative research, Bull. Amer. Meteor. Soc., 94, 1339–1360, https://doi.org/10.1175/BAMS-D-12-00121.1, 2013.

Jacobson, A. R., Gruber, N., Sarmiento, J. L., Gloor, M. and Fletcher, S. E. M.: A joint atmosphere-ocean inversion for surface fluxes of carbon dioxide: I. methods and global-scale fluxes, Global. Biogeochem. Cy., 21, GB1020, https://doi.org/10.1029/2005GB002556, 2007.

Jacobson, A. R., Schuldt, K. N., Tans, P., Arlyn Andrews, Miller, J. B., Oda, T., Mund, J., Weir, B., Ott, L., Aalto, T., Abshire, J. B., Aikin, K., Aoki, S., Apadula, F., Arnold, S., Baier, B., Bartyzel, J., Beyersdorf, A., Biermann, T., Biraud, S. C., Boenisch, H., Brailsford, G., Brand, W. A., Chen, G., Huilin Chen, Lukasz Chmura, Clark, S., Colomb, A., Commane, R., Conil, S., Couret, C., Cox, A., Cristofanelli, P., Cuevas, E., Curcoll, R., Daube, B., Davis, K. J., Wekker, S. de, Della Coletta, J., Delmotte, M., DiGangi, E., DiGangi, J. P., Di Sarra, A. G., Dlugokencky, E., Elkins, J. W., Emmenegger, L., Shuangxi Fang, Fischer, M. L., Forster, G., Frumau, A., Galkowski, M., Gatti, L. V., Gehrlein, T., Gerbig, C., Francois Gheusi, Gloor, E., Gomez-Trueba, V., Goto, D., Griffis, T., Hammer, S., Hanson, C., Haszpra, L., Hatakka, J., Heimann, M., Heliasz, M., Hensen, A., Hermansen, O., Hintsa, E., Holst, J., Ivakhov, V., Jaffe, D. A., Jordan, A., Joubert, W., Karion, A., Kawa, S. R., Kazan, V., Keeling, R. F., Keronen, P., Kneuer, T., Kolari, P., Kateřina Komínková, Kort, E., Kozlova, E., Krummel, P., Kubistin, D., Labuschagne, C., Lam, D. H., Lan, X., Langenfelds, R. L., Laurent, O., Laurila, T., Lauvaux, T., Lavric, J., Law, B. E., Lee, J., Lee, O. S., Lehner, I., Lehtinen, K., Leppert, R., Leskinen, A., Leuenberger, M., Levin, I., Levula, J., Lin, J., Lindauer, M., Loh, Z., Lopez, M., Luijkx, I. T., Lunder, C. R., Machida, T., Mammarella, I., Manca, G., Manning, A., Manning, A., Marek, M. V., Martin, M. Y., Matsueda, H., McKain, K., Meijer, H., Meinhardt, F., Merchant, L., N. Mihalopoulos, Miles, N. L., Miller, C. E., Mitchell, L., Mölder, M., Montzka, S., Moore, F., Moossen, H., Morgan, E., Josep-Anton Morgui, Morimoto, S., Müller-Williams, J., J. William Munger, Munro, D., Myhre, C. L., Shin-Ichiro Nakaoka, Jaroslaw Necki,

Newman, S., Nichol, S., Niwa, Y., Obersteiner, F., O'Doherty, S., Paplawsky, B., Peischl, J., Peltola, O., Piacentino, S., Jean-Marc Pichon, Pickers, P., Piper, S., Pitt, J., Plass-Dülmer, C., Platt, S. M., Prinzivalli, S., Ramonet, M., Ramos, R., Reyes-Sanchez, E., Richardson, S. J., Riris, H., Rivas, P. P., Ryerson, T., Saito, K., Sargent, M., Sasakawa, M., Scheeren, B., Schuck, T., Schumacher, M., Seifert, T., Sha, M. K., Shepson, P., Shook, M., Sloop, C. D., Smith, P., Stanley, K., Steinbacher, M., Stephens, B., Sweeney, C., Thoning, K., Timas, H., Torn, M., Tørseth, K., Trisolino, P., Turnbull, J., van den Bulk, P., van Dinther, D., Vermeulen, A., Viner, B., Vitkova, G., Walker, S., Watson, A., Wofsy, S. C., Worsey, J., Worthy, D., Dickon Young, Zaehle, S., Zahn, A., and Zimnoch, M.: CarbonTracker CT2022, Model published by NOAA Global Monitoring Laboratory, https://doi.org/10.25925/z1gj-3254 (last access: 20 May 2026), 2023.

Jin, C. X., Zhou, T. J., Chen, X. L., and Wu, B: Seasonally evolving dominant interannual variability mode of air–sea CO_2 flux over the western North Pacific simulated by CESM1-BGC, Sci. China Earth Sci. 60, 1854–1865, https://doi.org/10.1007/s11430-015-9085-4, 2017.

Johansson, M. M., Björkqvist, J.-V., Särkkä, J., Leijala, U., and Kahma, K. K.: Correlation of wind waves and sea level variations on the coast of the seasonally ice-covered Gulf of Finland, Nat. Hazards Earth Syst. Sci., 22, 813–829, https://doi.org/10.5194/nhess-22-813-2022, 2022.

Koseki, S., Tjiputra, J., Fransner, F., Crespo, L. R., and Keenlyside, N. S.: isentangling the impact of Atlantic Niño on sea–air CO_2 flux. Nat. Commun. 14, 3649, https://doi.org/10.1038/s41467-023-38718-9, 2023.

Krall, K. E., Smith, A. W., Takagaki, N., and Jähne, B.: Air–sea gas exchange at wind speeds up to 85 m s^{-1}, Ocean Sci., 15, 1783–1799, https://doi.org/10.5194/os-15-1783-2019, 2019.

Lan, Y.-Y., Hsu, H.-H., Tsuang, B.-J., and Tu, C.-Y.: rceclccr/CAM5_SIT_v1.0 (v1.0.0), Zenodo [code], https://doi.org/10.5281/zenodo.5510795, 2021.

Lan, Y.-Y.: POP2–waves coupled model in CESM1.2.2 framework, Zenodo [code], https://doi.org/10.5281/zenodo.15795234, 2025.

Li, S, Babanin, A. V., and Guan, C.: Dimensionless Parameterizations of Air–Sea CO_2 Gas Transfer Velocity on Surface Waves, Tellus B: Chem. Phys. Meteorol., 75(1), 1–12, https://doi.org/10.16993/tellusb.1867, 2023.

Liu, B., Six, K. D., and Ilyina, T.: Incorporating the stable carbon isotope 13C in the ocean biogeochemical component of the Max Planck Institute Earth System Model, Biogeosciences, 18, 4389–4429, https://doi.org/10.5194/bg-18-4389-2021, 2021.

Long, M. C., Lindsay, K., Peacock, S., Moore, J. K., and Doney, S. C.: Twentieth-Century oceanic carbon uptake and storage in CESM1 (BGC), J. Climate, 26, 6775–6800, https://doi.org/10.1175/JCLI-D-12-00184.1, 2013.

Lovato, T., Peano, D., Butenschön, M., Materia, S., Iovino, D., Scoccimarro, E., Fogli, P. G., Cherchi, A., Bellucci, A., Gualdi, S., Masina, S., and Navarra, A.: CMIP6 Simulations With the CMCC Earth System Model (CMCC-ESM2), J. Adv. Model. Earth Sy., 14, e2021MS002814, https://doi.org/10.1029/2021MS002814, 2022.

Lovenduski, N. S., Yeager, S. G., Lindsay, K., and Long, M. C.: Predicting near-term variability in ocean carbon uptake, Earth Syst. Dynam., 10, 45–57, https://doi.org/10.5194/esd-10-45-2019, 2019.

Macovei, V. A., Petersen, W., Brix, H., and Voynova, Y. G.: Reduced ocean carbon sink in the south and central North Sea (2014–2018) revealed from FerryBox observations Geophys. Res. Lett., 48, e2021GL092645, https://doi.org/10.1029/2021GL092645, 2021.

Mauritsen, T., Bader, J., Becker, T., Behrens, J., Bittner, M., Brokopf, R., Brovkin, V., Claussen, M., Crueger, T., Esch, M., Fast, I., Fiedler, S., Flaeschner, D., Gayler, V., Giorgetta, M., Goll, D. S., Haak, H., Hagemann, S., Hedemann, C., Hohenegger, C., Ilyina, T., Jahns, T., Jimenéz-de-la Cuesta, D., Jungclaus, J., Kleinen, T., Kloster, S., Kracher, D., Kinne, S., Kleberg, D., Lasslop, G., Kornblueh, L., Marotzke, J., Matei, D., Meraner, K., Mikolajewicz, U., Modali, K., Moebis, B., Mueller, W. A., Nabel, J. E. M. S., Nam, C. C. W., Notz, D., Nyawira, S.-S., Paulsen, H., Peters, K., Pincus, R., Pohlmann, H., Pongratz, J., Popp, M., Raddatz, T. J., Rast, S., Redler, R., Reick, C. H., Rohrschneider, T., Schemann, V., Schmidt, H., Schnur, R., Schulzweida, U., Six, K. D., Stein, L., Stemmler, I., Stevens, B., von Storch, J.-S., Tian, F., Voigt, A., Vrese, P., Wieners, K.-H., Wilkenskjeld, S., Winkler, A., and Roeckner, E.: Developments in the MPI-M Earth System Model version 1.2 (MPI-ESM1.2) and Its Response to Increasing CO_2, J. Adv. Model. Earth Sy., 11, 998–1038, https://doi.org/10.1029/2018MS001400, 2019.

McKinley, G. A., Fay, A. R., Eddebbar, Y. A., Gloege, L., and Lovenduski, N. S.: External forcing explains recentdecadal variability of the ocean carbonsink, AGU Advances, 1,e2019AV00014, https://doi.org/10.1029/2019AV000149, 2020.

Mellor, G. L., Donelan, M. A., and Oey, L.-Y.: A surface wave model for coupling with numerical ocean circulation models. J. Atmos. Ocean. Technol., 25(10), 1785–1807, https://doi.org/10.1175/2008JTECHO573.1, 2008.

Monahan, E. C., and Spillane, M. C.: The role of oceanic whitecaps in air–sea gas exchange, in: Gas transfer at water surfaces, edited by: Brutsaert, W. and Jirka, G. H., Reidel, Hingham, MA, 495–503, https://doi.org/10.1007/978-94-017-1660-4_45, 1984.

Moore, J. K., Lindsay, K., Doney, S. C., Long, M. C., and Misumi, K.: Marine ecosystem dynamics and biogeochemical cycling in the Community Earth System Model [CESM1 (BGC)]: Comparison of the 1990s with the 2090s under the RCP4. 5 and RCP8. 5 scenarios, J. Climate, 26, 9291–9312, https://doi.org/10.1175/JCLI-D-12-00566.1, 2013.

Müller, J. D., Gruber, N., Carter, B., Feely, R., Ishii, M., Lange, N., Lauvset, S. K., Murata, A., Olsen, A., Pérez, F. F., Sabine, C., Tanhua, T., Wanninkhof, R., and Zhu, D.: Decadal trends in the oceanic storage of anthropogenic carbon from 1994 to 2014. AGU Advances, 4, e2023AV000875, https://doi.org/10.1029/2023AV000875, 2023.

Reichl, B. G., and Deike, L.: Contribution of Sea-State Dependent Bubbles to Air–sea Carbon Dioxide Fluxes, Geophys. Res. Lett., 47, e2020GL087267. https://doi.org/10.1029/2020GL087267, 2020.

Roobaert, A., Resplandy, L., Laruelle, G. G., Liao, E., and Regnier, P.: Unraveling the physical and biological controls of the global coastal CO_2 sink, Global Biogeochem. Cy., 38, e2023GB007799. https://doi.org/10.1029/2023GB007799, 2024.

Rustogi, P., Resplandy, L., Liao, E., Reichl, B. G., and Deike, L.: Influence of wave-induced variability on ocean carbon uptake. Global Biogeochem. Cy., 39, e2024GB008382. https://doi.org/10.1029/2024GB008382, 2025.

Sabine, C., Sutton, A., McCabe, K., Lawrence-Slavas, N., Alin, S, Feely, R., Jenkins, R., Maenner, S., Meinig, C., Thomas, J., van Ooijen, E., Passmore, A., and Tilbrook, B.: Evaluation of a new carbon dioxide system for autonomous surface vehicles, J. Atmos. Oceaen. Tech., 37, 1305–1317, https://doi.org/10.1175/JTECH-D-20-0010.1, 2020.

Séférian, R., Nabat, P., Michou, M., Saint-Martin, D., Voldoire, A., Colin, J., Decharme, B., Delire, C., Berthet, S., Chevallier, M., Sénési, S., Franchisteguy, L., Vial, J., Mallet, M., Joetzjer, E., Geoffroy, O., Guérémy, J.-F., Moine, M.-P., Msadek, R., Ribes, A., Rocher, M., Roehrig, R., Salas-y-Mélia, D., Sanchez, E., Terray, L., Valcke, S., Waldman, R., Aumont, O., Bopp, L., Deshayes, J., Éthé, C., and Madec, G.: Evaluation of CNRM Earth-System model, CNRM-ESM2-1: role of Earth system processes in present-day and future climate, J. Adv. Model. Earth Sy., 11, 4182–4227, https://doi.org/10.1029/2019MS001791, 2019.

Séférian, R., Berthet, S., SGO, Y., Bopp, L., Gehlen, M., and Joos, F.: Assessment of ocean carbon cycle models in the JULES-OM2 configurations, Geosci. Model Dev., 13, 4521–4543, https://doi.org/10.5194/gmd-13-4521-2020, 2020.

Seland, Ø., Bentsen, M., Olivié, D., Toniazzo, T., Gjermundsen, A., Graff, L. S., Debernard, J. B., Gupta, A. K., He, Y.-C., Kirkevåg, A., Schwinger, J., Tjiputra, J., Aas, K. S., Bethke, I., Fan, Y.,

1207 Griesfeller, J., Grini, A., Guo, C., Ilicak, M., Karset, I. H. H.,
1208 Landgren, O., Liakka, J., Moseid, K. O., Nummelin, A., Spensberger,
1209 C., Tang, H., Zhang, Z., Heinze, C., Iversen, T., and Schulz, M.:
1210 Overview of the Norwegian Earth System Model (NorESM2) and key
1211 climate response of CMIP6 DECK, historical, and scenario
1212 simulations, Geosci. Model Dev., 13, 6165–6200,
1213 https://doi.org/10.5194/gmd-13-6165-2020, 2020.

1214 Sellar, A. A., Jones, C. G., Mulcahy, J. P., Tang, Y., Yool, A., Wiltshire,
1215 A., O'Connor, F. M., Stringer, M., Hill, R., Palmieri, J., Woodward,
1216 S., de Mora, L., Kuhlbrodt, T., Rumbold, S. T., Kelley, D. I., Ellis,
1217 R., Johnson, C. E., Walton, J., Abraham, N. L., Andrews, M. B.,
1218 Andrews, T., Archibald, A. T., Berthou, S., Burke, E., Blockley, E.,
1219 Carslaw, K., Dalvi, M., Edwards, J., Folberth, G. A., Gedney, N.,
1220 Griffiths, P. T., Harper, A. B., Hendry, M. A., Hewitt, A. J., Johnson,
1221 B., Jones, A., Jones, C. D., Keeble, J., Liddicoat, S., Morgenstern,
1222 O., Parker, R. J., Predoi, V., Robertson, E., Siahaan, A., Smith, R.
1223 S., Swaminathan, R., Woodhouse, M. T., Zeng, G., and Zerroukat,
1224 M.: UKESM1: Description and Evaluation of the U.K. Earth System
1225 Model, J. Adv. Model. Earth Syst., 11, 4513–4558,
1226 https://doi.org/10.1029/2019MS001739, 2019.

1227 Shutler, J. D., Wanninkhof, R., Nightingale, P. D., Woolf, D. K., Bakker,
1228 D. C., Watson, A., Ashton, I., Holding, T., Chapron, B., Quilfen, Y.,
1229 Fairall, C., Schuster, U., Nakajima, M., and Donlon, C. J.: Satellites
1230 will address critical science priorities for quantifying ocean carbon,
1231 Front. Ecol. Environ., 18(1): 27–35,
1232 http://dx.doi.org/10.1002/fee.2129, 2019.

1233 Sigmond, M., Anstey, J., Arora, V., Digby, R., Gillett, N., Kharin, V.,
1234 Merryfield, W., Reader, C., Scinocca, J., Swart, N., Virgin, J.,
1235 Abraham, C., Cole, J., Lambert, N., Lee, W.-S., Liang, Y., Malinina,
1236 E., Rieger, L., von Salzen, K., Seiler, C., Seinen, C., Shao, A.,
1237 Sospedra-Alfonso, R., Wang, L., and Yang, D.: Improvements in the
1238 Canadian Earth System Model (CanESM) through systematic model
1239 analysis: CanESM5.0 and CanESM5.1, Geosci. Model Dev., 16,
1240 6553–6591, https://doi.org/10.5194/gmd-16-6553-2023, 2023.

1241 Signorini, S. R., and McClain, C. R.: Effect of uncertainties in
1242 climatologic wind, ocean pCO_2, and gas transfer algorithms on the
1243 estimate of global sea–air CO_2 flux, Global Biogeochem. Cy., 23,
1244 GB2025, https://doi.org/10.1029/2008GB003246, 2009.

1245 Smith, R., Jones, P., Briegleb, B., Bryan, F., Danabasoglu, G., Dennis,
1246 J., Dukowicz, J., Eden, C., Fox-Kemper, B., Gent, P., Hecht, M.,
1247 Jayne, S., Jochum, M., Large, W., Lindsay, K., Maltrud, M., Norton,
1248 N., Peacock, S., Vertenstein, M., and Yeager, S.: The Parallel Ocean
1249 Program (POP) reference manual ocean component of the
1250 Community Climate System Model (CCSM) and Community Earth
1251 System Model (CESM), Los Alamos National Laboratory Tech. Rep.
1252 LAUR-10-01853, 140 pp,
1253 https://www2.cesm.ucar.edu/models/cesm1.0/pop2/doc/sci/POPRef

Manual.pdf, 2010.

Soloviev, A., and Lukas, R.: Effects of Bubbles and Sea Spray on Air–Sea Exchange in Hurricane Conditions, Bound.-Layer Meteorol., 136, 365–376, https://doi.org/10.1007/s10546-010-9505-0, 2010.

Stock, C. A., Dunne, J. P., Fan, S., Ginoux, P., John, J., Krasting, J. P., Laufkötter, C., Paulot, F., and Zadeh, N.: Ocean biogeochemistry in GFDL's Earth System Model 4.1 and its response to increasing atmospheric CO_2, J. Adv. Model. Earth Sy., 12, e2019MS002043, https://doi.org/10.1029/2019MS002043, 2020.

Sutton, A. J., Sabine, C. L., Maenner-Jones, S., Lawrence-Slavas, N., Meinig, C., Feely, R. A., Mathis, J. T., Musielewicz, S., Bott, R., McLain, P. D., Fought, H. J., and Kozyr, A.: A high-frequency atmospheric and seawater pCO_2 data set from 14 open-ocean sites using a moored autonomous system, Earth Syst. Sci. Data, 6, 353–366, https://doi.org/10.5194/essd-6-353-2014, 2014.

Tjiputra, J. F., Schwinger, J., Bentsen, M., Morée, A. L., Gao, S., Bethke, I., Heinze, C., Goris, N., Gupta, A., He, Y.-C., Olivié, D., Seland, Ø., and Schulz, M.: Ocean biogeochemistry in the Norwegian Earth System Model version 2 (NorESM2), Geosci. Model Dev., 13, 2393–2431, https://doi.org/10.5194/gmd-13-2393-2020, 2020.

Tokoro, T., Hosokawa, S., Miyoshi, E., Tada, K., Watanabe, K., Montani, S., Kayanne, H., and Kuwae, T.: Net uptake of atmospheric CO_2 by coastal submerged aquatic vegetation, Glob. Change Biol., 20, 1873–1884, https://doi.org/10.1111/gcb.12543, 2014.

Van Dam, B., Polsenaere, P., Barreras-Apodaca, A., Lopes, C., Sanchez-Mejia, Z., Tokoro, T., Kuwae, T., Loza, L. G., Rutgersson, A., Fourqurean, J., and Thomas, H.: Global trends in air-water CO_2 exchange over seagrass meadows revealed by atmospheric Eddy Covariance, Global Biogeochem. Cy., 35, e2020GB006848, https://doi.org/10.1029/2020GB006848, 2021.

Wanninkhof, R.: Relationship between wind speed and gas exchange over the ocean, J. Geophys. Res., 97(C5), 7373–7382. https://doi.org/10.1029/92JC00188, 1992.

Wanninkhof, R.: Relationship between wind speed and gas exchange over the ocean revisited, Limnol. Oceanogr.: Methods, 12(6), 351–362. https://doi.org/10.4319/lom.2014.12.351, 2014.

Weiss, R. F.: Carbon dioxide in water and seawater: the solubility of a non-ideal gas, Mar. Chem., 2 (3), pp. 203-215, https://doi.org/10.1016/0304-4203(74)90015-2, 1974.

Williams, N. L., Juranek, L. W., Feely, R. A., Johnson, K. S., Sarmiento, J. L., Talley, L. D., Dickson, A. G., Gray, A. R., Wanninkhof, R., Russell, J. L., and Riser, S. C.: Calculating surface ocean pCO_2 from biogeochemical Argo floats equipped with pH: An uncertainty analysis, Global Biogeochem. Cy., 31, 591–604,

https://doi.org/10.1002/2016GB005541, 2017.

Wu, Y., and Qi, D.: The controversial Southern Ocean air–sea CO_2 flux in the era of autonomous ocean observations, Sci. Bull., 68, 21, 2519-2522, https://doi.org/10.1016/j.scib.2023.08.059, 2023.

Wu, L., Cai, Y., and Rutgersson, A.: Ocean surface waves impact on global air–sea CO_2 flux, Biogeochem., 168, 68, https://doi.org/10.1007/s10533-025-01267-y, 2025.

Yang, X., Wynn-Edwards, C. A., Strutton, P. G., and Shadwick, E. H.: Drivers of air–sea CO_2 flux in the subantarctic zone revealed by time series observations. Global Biogeochem. Cy., 38, e2023GB007766, https://doi.org/10.1029/2023GB007766, 2024.

Yool, A., Palmiéri, J., Jones, C. G., de Mora, L., Kuhlbrodt, T., Popova, E. E., Nurser, A. J. G., Hirschi, J., Blaker, A. T., Coward, A. C., Blockley, E. W., and Sellar, A. A.: Evaluating the physical and biogeochemical state of the global ocean component of UKESM1 in CMIP6 historical simulations, Geosci. Model Dev., 14, 3437–3472, https://doi.org/10.5194/gmd-14-3437-2021, 2021.

Zhou, X., Reichl, B. G., Romero, L., and Deike, L.: A sea state dependent gas transfer velocity for CO_2 unifying theory, model, and field data, Earth Space Sci., 10, e2023EA003237, https://doi.org/10.1029/2023EA003237, 2023.

Ziehn, T., Chamberlain, M., Law, R., Lenton, A., Bodman, R., Dix, M., Stevens, L., Wang, Y.-P., and Srbinovsky, J.: The Australian Earth System Model: ACCESS-ESM1.5, J. South. Hemisph. Earth Syst. Sci., 70(1) 193-214, https://doi.org/10.1071/ES19035, 2020.

Table 1. Characteristics of the 12 key regions exhibiting prominent air–sea CO_2 flux variability across the three major ocean basins.

Basins	Key regions
the Pacific Ocean	the Northwestern Pacific (NWP), Eastern Equatorial Pacific (EEP), Northeastern Pacific (NEP), South Pacific Ocean 1 (SPO1), and South Pacific Ocean 2 (SPO2)
the Indian Ocean	the North Indian Ocean (NIO), South Indian Ocean 1 (SIO1), and South Indian Ocean 2 (SIO2)
the Atlantic Ocean	the North Atlantic Ocean 1 (NAO1), North Atlantic Ocean 2 (NAO2), Equatorial Atlantic Ocean (EAO), and South Atlantic Ocean (SAO)

Table 2. Intercomparison of Earth System Model for estimating air–sea CO_2 flux

Earth System Model	**Ocean components**	**Wave-informed air–sea CO_2 flux**	**$k_{w,660}$ parameterization**	**Reference**
CESM1[1]	POP2[2]	no	U_{10} (Wannikhof 1992)	Chikamoto and DiNezio, 2021; Chikamoto et al., 2023
CESM2[3]	POP2[2]	no	U_{10} (Wannikhof 2014)	Danabasoglu et al., 2020
NorESM2[4]	BLOM[5]	no	U_{10} (Wannikhof 2014)	Seland et al., 2020; Tjiputra et al., 2020
MPI-ESM1.2[6]	MPIOM 1.6[7]	no	U_{10} (Wannikhof 2014)	Mauritsen et al., 2019; Liu et al., 2021
ACCESS-ESM1.5[8]	MOM5[9]	no	U_{10} (Wannikhof 1992)	Ziehn et al., 2020
CMCC-ESM2[10]	NEMO v3.6[11]	no	U_{10} (Wannikhof 1992)	Lovato et al., 2022
CanESM5[12]	CanNEMO[13]	no	U_{10} (Wannikhof 1992)	Sigmond et al., 2023
GFDL-ESM4.1[14]	MOM6[15]	no	U_{10} (Wannikhof 2014)	Stock et al., 2020; Roobaert et al., 2024
IPSL-CM6A-LR[16]	NEMO-PISCES[17]	no	U_{10} (Wannikhof 1992)	Boucher et al., 2020
MIROC-ES2L[18]	COCO 4.0[19]	no	U_{10} (Wannikhof 1992)	Hajima et al., 2020
UKESM1[20]	NEMO v3.6[11]	no	U_{10} (Wannikhof 1992)	Sellar et al., 2019; Yool et al., 2021
CNRM-ESM2-1[21]	NEMO-PISCES[17]	no	U_{10} (Wannikhof 1992)	Séférian et al., 2019
-[22]	NEMO-PISCES[17]	Yes	H_s, u^* (Deike and Melville, 2018)	Wu et al., 2025
-[22]	MOM6-COBALTv2[23]	Yes	H_s, u^* (Deike and Melville, 2018)	Rustogi et al., 2025
CESM1-POP2–waves[24]	POP2–waves coupled model	Yes	H_s, u^* (Deike and Melville, 2018)	This study

Note:

[1]CESM1: the Community Earth System Model version 1 of the National Center for Atmospheric Research (NCAR);

[2]POP2: the Parallel Ocean Program version 2 of NCAR;

[3]CESM2: CESM version 2;

[4]NorESM2: The Norwegian Earth System Model version 2;

[5]BLOM: Bergen Layered Ocean Model;
[6]MPI-ESM1.2: the Max Planck Institute for Meteorology Earth System Model version 1.2;
[7]MPIOM 1.6: the Max-Planck Institute Ocean Model version 1.6;
[8]ACCESS-ESM1.5: the Australian Community Climate and Earth System Simulator form an Earth System Model version 1.5;
[9]MOM5: the GFDL Modular Ocean Model version 5;
[10]CMCC-ESM2: the Euro-Mediterranean Centre on Climate Change (CMCC) Earth System Model version 2;
[11]NEMO v3.6: Nucleus for European Modelling of the Ocean version 3.6;
[12]CanESM5: the Canadian Earth System Model version 5;
[13]CanNEMO: NEMO version 3.4 modified for CanESM;
[14]GFDL-ESM4.1: the Geophysical Fluid Dynamics Laboratory's Earth System Model 4.1;
[15]MOM6: the GFDL Modular Ocean Model version 6;
[16]IPSL-CM6A-LR : version 6 of the Institut Pierre-Simon Laplace (IPSL) climate model;
[17]NEMO-PISCES: Nucleus for European Modelling of the Ocean, Pelagic Interaction Scheme for Carbon and Ecosystem Studies ocean general circulation and biogeochemistry model;
[18]MIROC-ES2L: the Model for Interdisciplinary Research on Climate, Earth System version 2;
[19]COCO 4.0: CCSR (Center for Climate System Research) Ocean Component Model version 4.0;
[20]UKESM1: the U.K. Earth System Model;
[21]CNRM-ESM2-1: the Earth system (ES) model of second generation developed by the Centre National de Recherches Météorologiques (CNRM);
[22]The simulations were conducted using global ocean-only models rather than full Earth System Models;
[23]MOM6-COBALTv2: Geophysical Fluid Dynamics Laboratory global ocean model (Modular Ocean Model, MOM6) coupled with sea ice and biogeochemistry (Carbon, Ocean Biogeochemistry and Lower Trophics version 2, COBALTv2);
[24]CESM1-POP2–waves: POP2–waves coupled model based on CESM1.

Table 3. Relative magnitudes of model–data biases (%), defined as the monthly mean absolute deviation normalized by the model's corresponding monthly variability range (95th minus 5th percentile)

Model	**NWP**	**EEP**	**NEP**	**SPO1**	**NIO**	**SIO1**	**NAO1**	**EAO**
POP2–waves	21.9	46.5	24.7	21.1	14.5	17.8	14.3	15.0
B–CTL (baseline)	26.8	71.5	25.3	22.1	16.2	21.9	15.4	11.9

Note:

Abbreviations: NWP: Northwestern Pacific; EEP: Eastern Equatorial Pacific; NEP: Northeastern Pacific; SPO1: South Pacific Ocean 1; NIO: North Indian Ocean; SIO1: South Indian Ocean 1; NAO1: North Atlantic Ocean 1; EAO: Equatorial Atlantic Ocean.

The relative magnitude of model–data bias (%) across the 360-month period is defined and calculated as follows:

$$\text{Model} - \text{data biases}\ (\%) = \frac{1}{12}\sum_{i=1}^{12}\frac{|Mi - Oi|}{P_{95}(M) - P_5(M)}$$

where *M*i and *O*i represent the monthly mean values simulated by (POP2–waves or B–CTL) and reference (the NOAA CT2022 inversion) air–sea CO_2 fluxes for the month mean of month i (i = 1, 2, …, 12), respectively. P_{95} (*M*) and P_5 (*M*) denote the 95th and 5th percentiles, respectively, of each calendar month's values over the 30-year period, representing the corresponding range of monthly variability in the model.

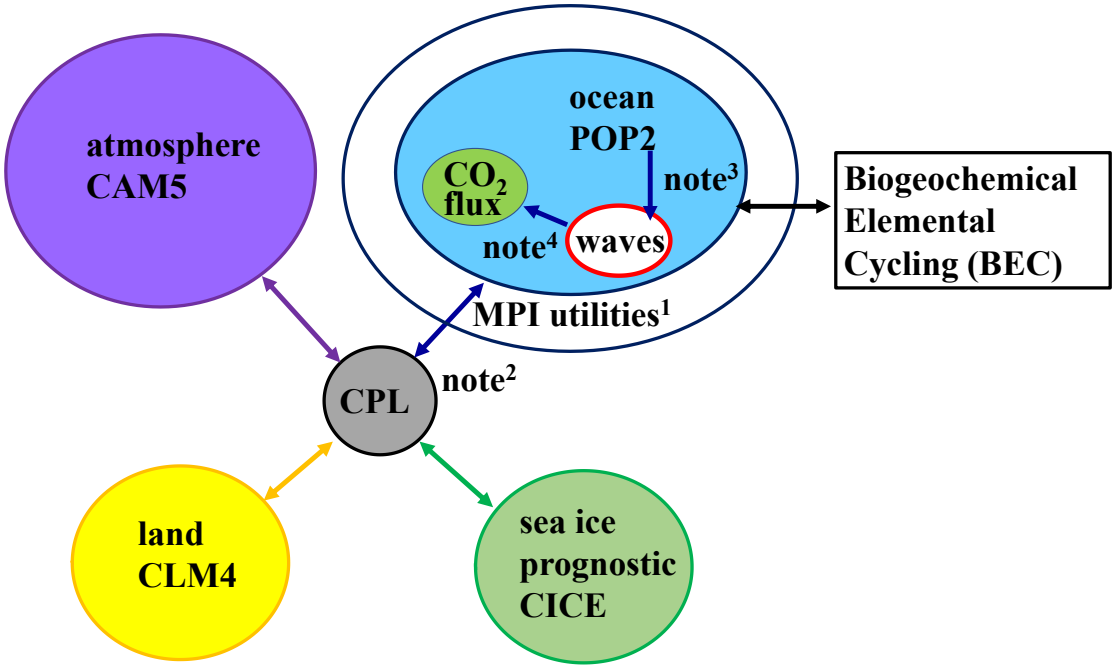

Figure 1. Architecture diagram for POP2–waves experiment in CESM1.2.2 framework, all components adhere to the CESM 1.2.2 framework, except for certain parts of the ocean component. The model components including components for the atmosphere [Community Atmosphere Model version 5 (CAM5)], land [Community Land Model version 4 (CLM4)], ocean [Parallel Ocean Program, version 2 (POP2)], along with its associated modules—the waves module (waves) and the Biogeochemical Elemental Cycling (BEC) module—sea ice [prognostic Los Alamos Sea Ice Model (CICE)], and the coupler (CPL).

Note:

[1]The wave-module variables are communicated between neighboring blocks via MPI, including zonal and meridional 10-m winds, wave radiation stress, subsurface momentum, and wave radiation and energy densities.

[2]To transfer variables such as zonal and meridional 10-m winds and friction velocity (including sea surface and ice fraction) from the CPL to POP2.

[3]The wave module receives variables from POP2, including the interpolation of depth-varying currents from z-coordinates (60 levels) to the wave module's vertical sigma coordinates (21 levels), along with ocean grid information in the x, y, and z directions.

[4]The wave module outputs significant wave height and friction velocity from the CPL for calculating the bubble-mediated gas transfer velocity in Eq. (3).

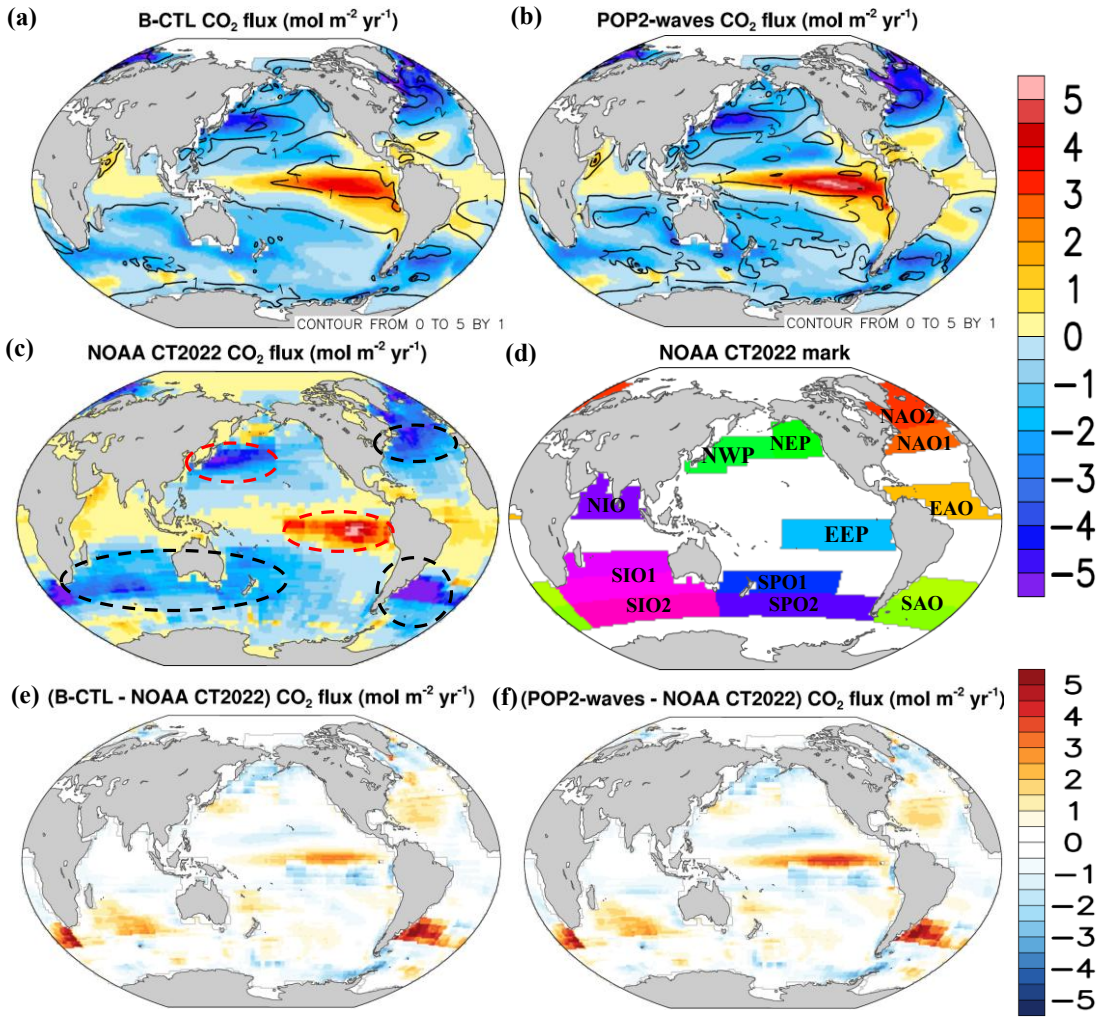

Figure 2. Climatological mean air–sea CO_2 flux (mol m^{-2} yr^{-1}; shaded) and monthly standard deviation (SD; contour): (a) B–CTL; (b) POP2–waves; (c) NOAA CT2022: red dashed lines highlight the primary oceanic CO_2 outgassing and uptake regions in the Pacific Ocean, while black dashed lines mark regions with an air–sea CO_2 flux below –2 mol m^{-2} yr^{-1}; (d) Based on NOAA CT2022, 12 key regions exhibiting significant air–sea CO_2 flux variability have been identified among the 30 ocean basins defined in the CT2022 model documentation (Jacobson et al., 2023) for optimizing flux inversions. These include: (1) Pacific Ocean: Northwestern Pacific (NWP), Eastern Equatorial Pacific (EEP), as well as Northeastern Pacific (NEP), South Pacific Ocean 1 (SPO1), and South Pacific Ocean 2 (SPO2); (2) Indian Ocean: North Indian Ocean (NIO), South Indian Ocean 1 (SIO1), and South Indian Ocean 2 (SIO2); (3) Atlantic Ocean: North Atlantic Ocean 1 (NAO1), North Atlantic Ocean 2 (NAO2), Equatorial Atlantic Ocean (EAO), and South Atlantic Ocean (SAO), (e) the air–sea CO_2 flux difference between B–CTL and NOAA CT2022, and (f) same as (e), but between POP2–waves and NOAA CT2022.

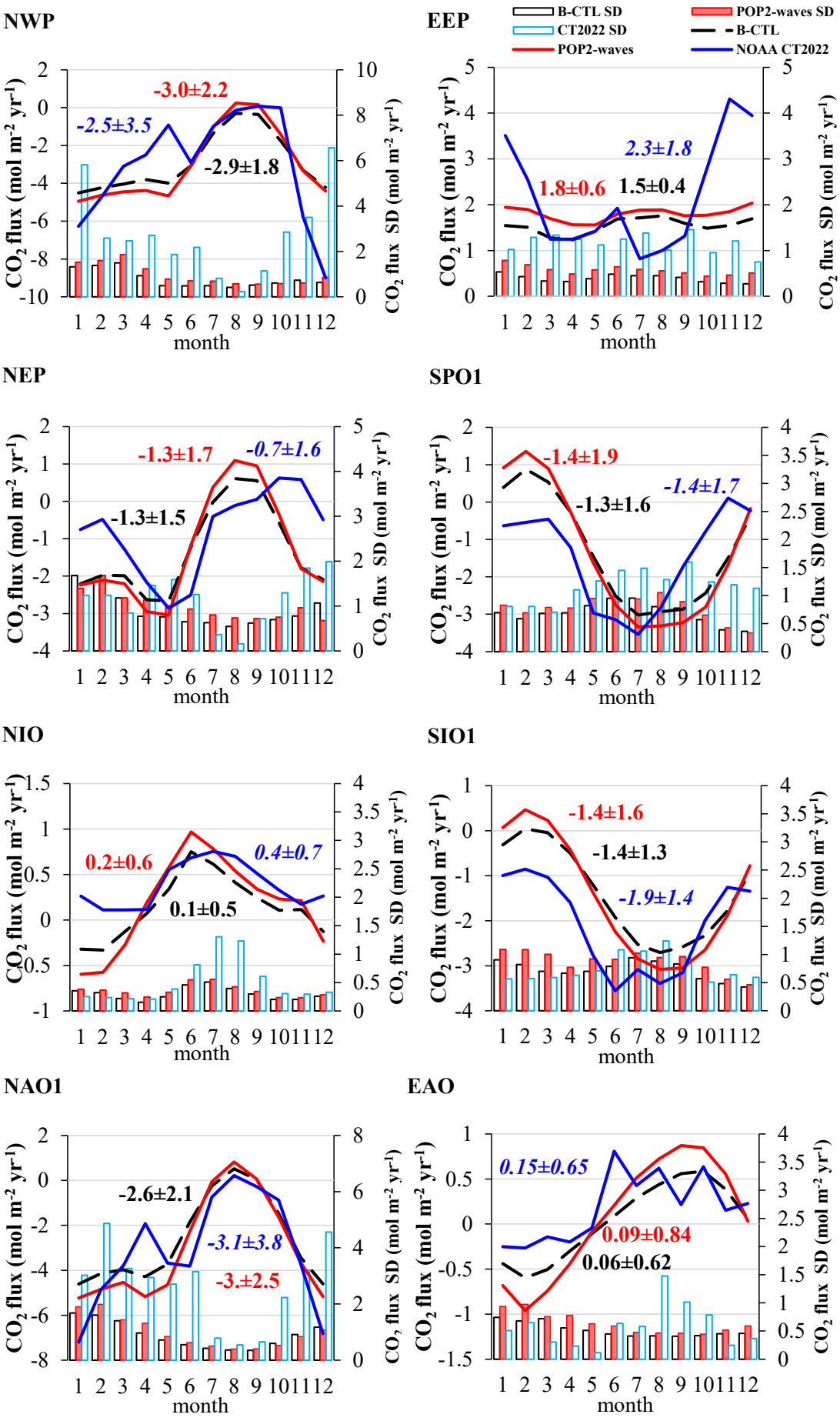
NWP
-3.0±2.2
-2.5±3.5
-2.9±1.8
EEP
B-CTL SD
CT2022 SD
POP2-waves
POP2-waves SD
B-CTL
NOAA CT2022
2.3±1.8
1.8±0.6
1.5±0.4
NEP
-1.3±1.7
-0.7±1.6
-1.3±1.5
SPO1
-1.4±1.9
-1.4±1.7
-1.3±1.6
NIO
0.2±0.6
0.4±0.7
0.1±0.5
SIO1
-1.4±1.6
-1.4±1.3
-1.9±1.4
NAO1
-2.6±2.1
-3.1±3.8
-3.±2.5
EAO
0.15±0.65
0.09±0.84
0.06±0.62
CO2 flux (mol m-2 yr-1)
CO2 flux SD (mol m-2 yr-1)
month

1423

Figure 3. Climatological monthly mean CO_2 flux for eight highly correlated regions defined in Fig. 2d (NWP, EEP, NEP, SPO1, NIO, SIO1, NAO1, and EAO). Lines indicate values for B–CTL (black dashed), POP2–waves (red solid), and NOAA CT2022 (blue solid). Regional-average values are distinguished by a black font for B–CTL, red font for POP2–waves, and blue italics for NOAA CT2022. Monthly standard deviation (SD) is shown as bars: black hollow (B–CTL), red solid (POP2–waves), and light blue hollow (NOAA CT2022).

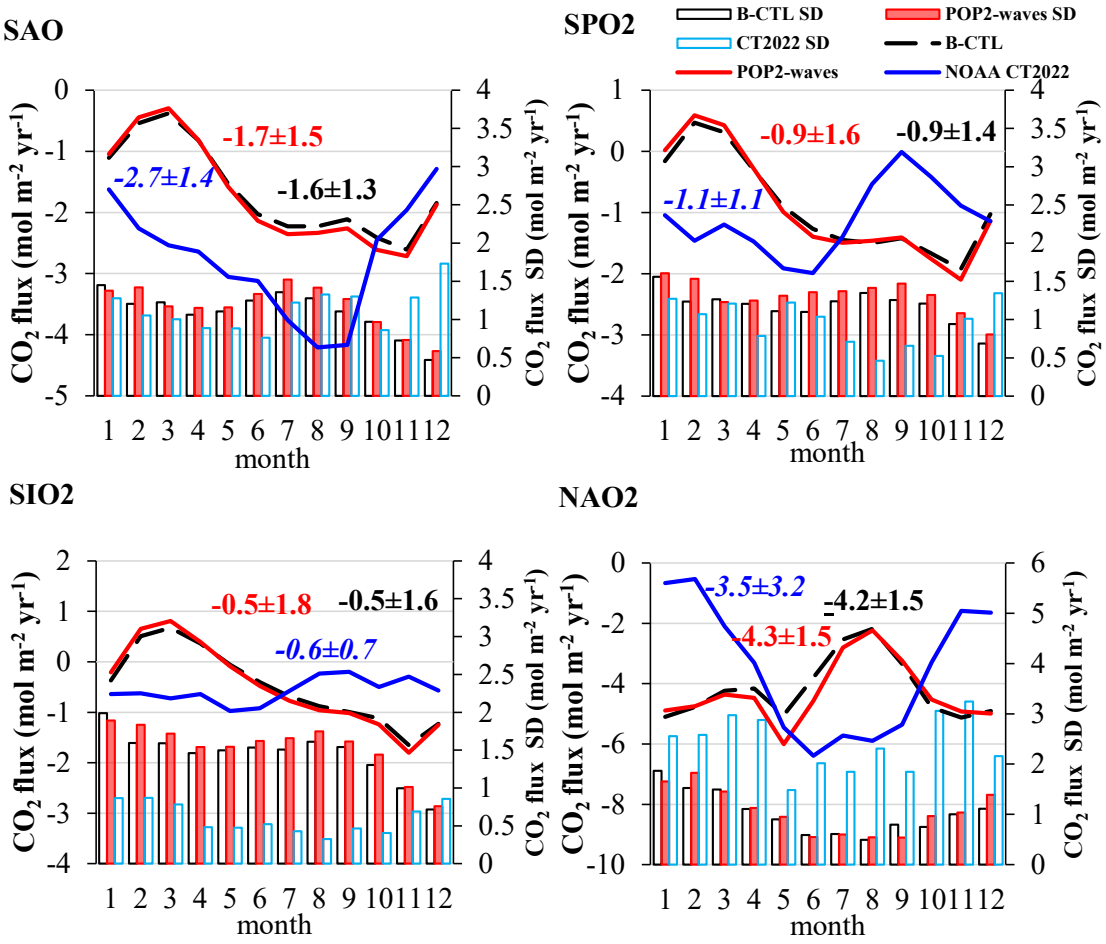

Figure 4. Same as Fig. 3, but for the four low-correlation characteristic regions (SAO, SPO2, SIO2, and NAO2), showing the climatological average of the simulated CO_2 flux compared with NOAA CT2022.

Note: SAO, South Atlantic Ocean; SPO2, South Pacific Ocean Region 2; SIO2, South Indian Ocean Region 2; NAO2, North Atlantic Ocean Region 2.

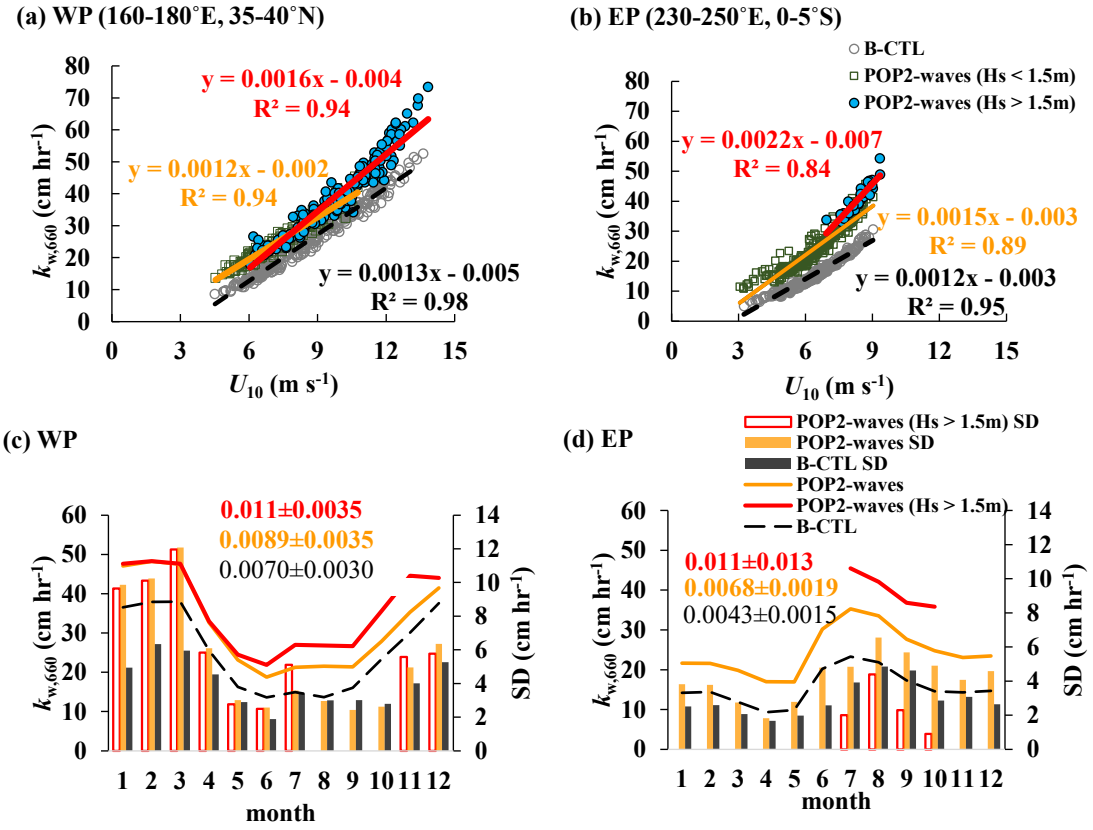

Figure 5. Scatter plots of monthly averaged gas transfer velocity ($k_{w,660}$) versus U_{10} for (a) the Western Pacific (WP; 160–180°E, 35–40°N) and (b) the Eastern Pacific (EP; 230–250°E, 0–5°S). Gray open circles, green open squares, and blue dots with black edges represent B–CTL, POP2–waves data for H_s < 1.5 m, and H_s > 1.5 m, respectively. Corresponding simple linear regressions (SLRs) and squared correlation coefficients (R^2) are shown with black dotted lines/text (B–CTL), orange solid lines/text (POP2–waves, H_s < 1.5 m), and red solid lines/text (POP2–waves, H_s > 1.5 m). Panels (c) and (d) display the monthly mean values of $k_{w,600}$ for WP and EP, respectively. Red and orange solid lines/text indicate POP2–waves (H_s > 1.5 m) and the average of all POP2–waves data, while the black dotted line/text represents B–CTL. The bar graph illustrates the standard deviation (SD) for each month over the WP and EP, red hollow bars for POP2–waves (H_s > 1.5 m), orange for average POP2–waves, and black for B–CTL.

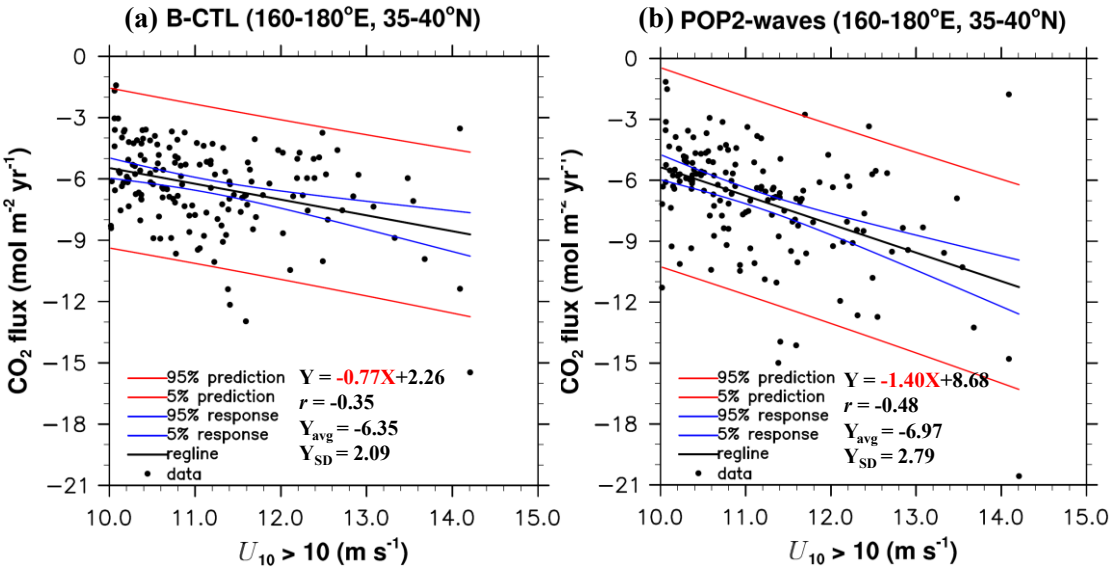

Figure 6. Scatter plots of air–sea CO_2 flux versus U_{10} with regression lines over the Western Pacific (160–180°E, 35–40°N) under high-wind conditions (U_{10} > 10 m s^{-1}) for (a) B–CTL and (b) POP2–waves experiments. Black dots indicate monthly mean values from each experiment. Blue lines denote the 95% and 5% confidence limits of the mean response, while red lines denote the 95% and 5% prediction intervals. The regression equation (Y = mx + b), Pearson correlation coefficient (*r*), mean CO_2 flux (Y_{avg}), and standard deviation (Y_{SD}) are shown to the right of the legend.

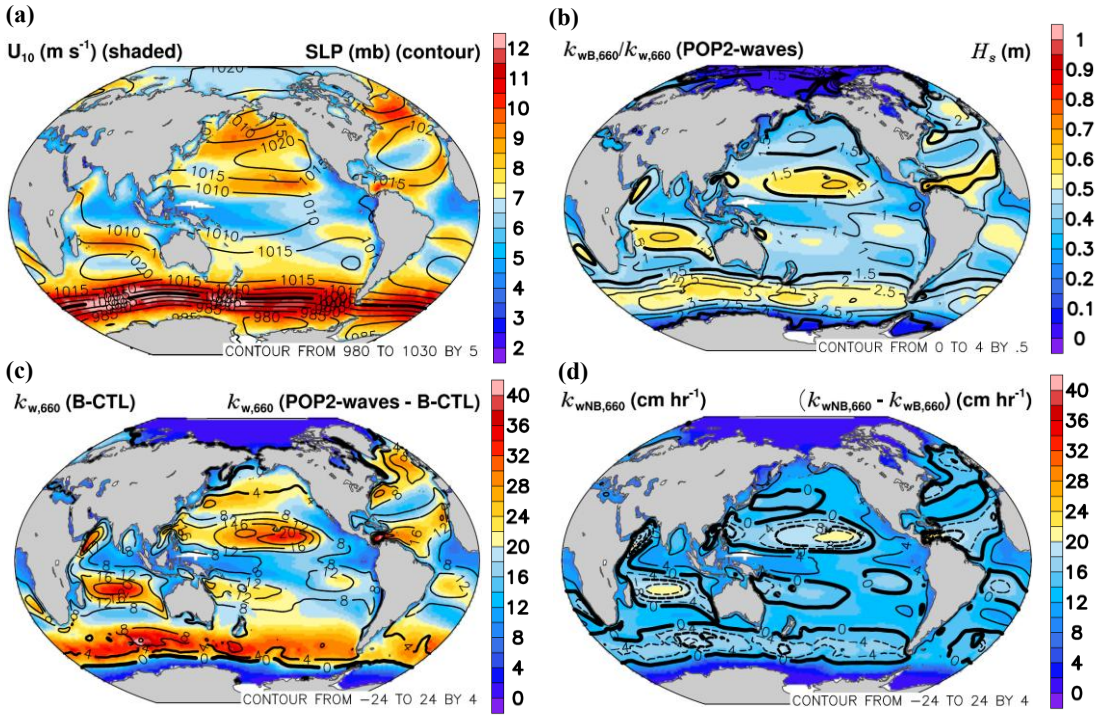

Figure 7. Effects of atmospheric factors and wave components on average gas transfer velocity: (a) Shaded areas represent 10-m wind speed (U_{10}, m s^{-1}) and contours show sea level pressure (SLP, mb); (b) color denotes the ratio of bubble-mediated ($k_{wB,660}$) to POP2–waves $k_{w,660}$ components, with contours representing significant wave height H_s (m) and thick lines marking H_s = 1.5 m; (c) shading represents $k_{w,660}$ (B–CTL) and contours represent the difference $k_{w,660}$ (POP2–waves − B–CTL) in cm hr^{-1}; (d) shading shows the non-bubble-mediated component ($k_{wNB,660}$) and contours show the difference ($k_{wNB,660} - k_{wB,660}$) in cm hr^{-1}, with the thick contour lines at 0.

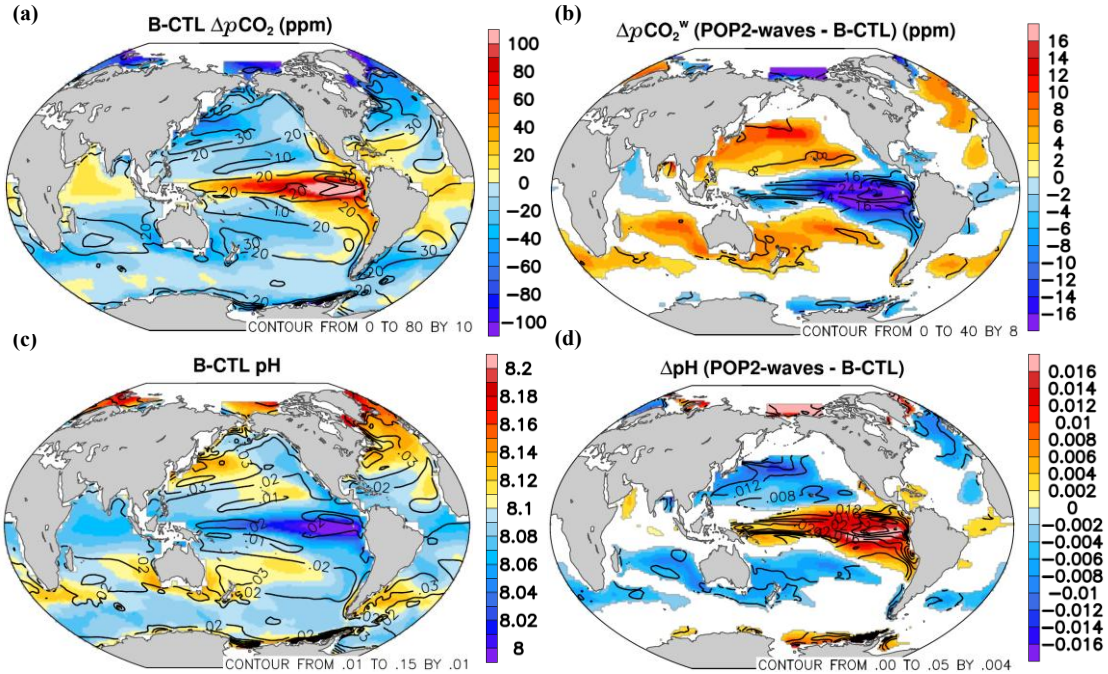

Figure 8. Spatial distributions of the 30-year climatological averages and model differences for ΔpCO_2^w (ppm; panels a, b) and ocean surface pH (panels c, d). Climatological means are represented by shading, and their corresponding standard deviation (SD) is superimposed as contours. Panels (a) and (c) present baseline results from the B–CTL simulation. Panels (b) and (d) depict the structural differences between the POP2–waves and B–CTL experiments (POP2–waves minus B–CTL), where stippling indicates statistical significance at the 95% confidence level based on a Student's t-test.

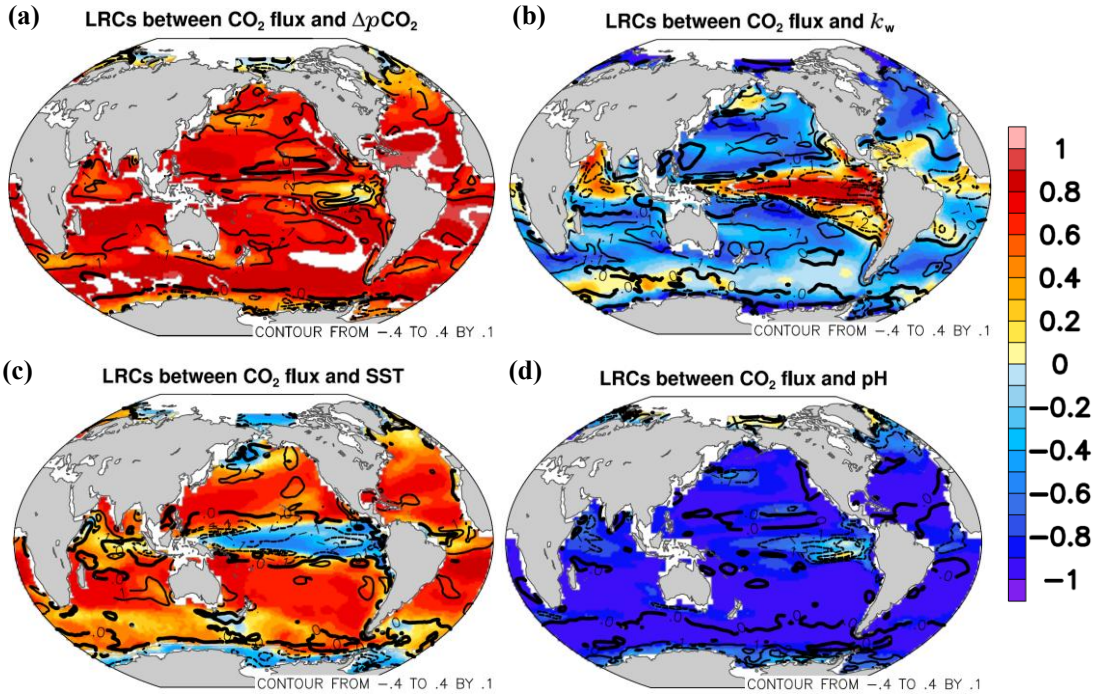

Figure 9. Spatial distributions of the 30-year averages of the linear regression coefficients (LRCs) between the CO_2 flux and (a) ΔpCO_2, ((b) $k_{w,660}$, (c) SST, and (d) pH. Shading represents the baseline LRCs from the B–CTL simulation, while overlaid contours depict the structural differences between the POP2–waves and B–CTL experiments (POP2–waves minus B–CTL). White areas denote regions where the LRCs are statistically insignificant at the 95% confidence level (based on a Student's t-test). All variables were standardized prior to the regression analysis.

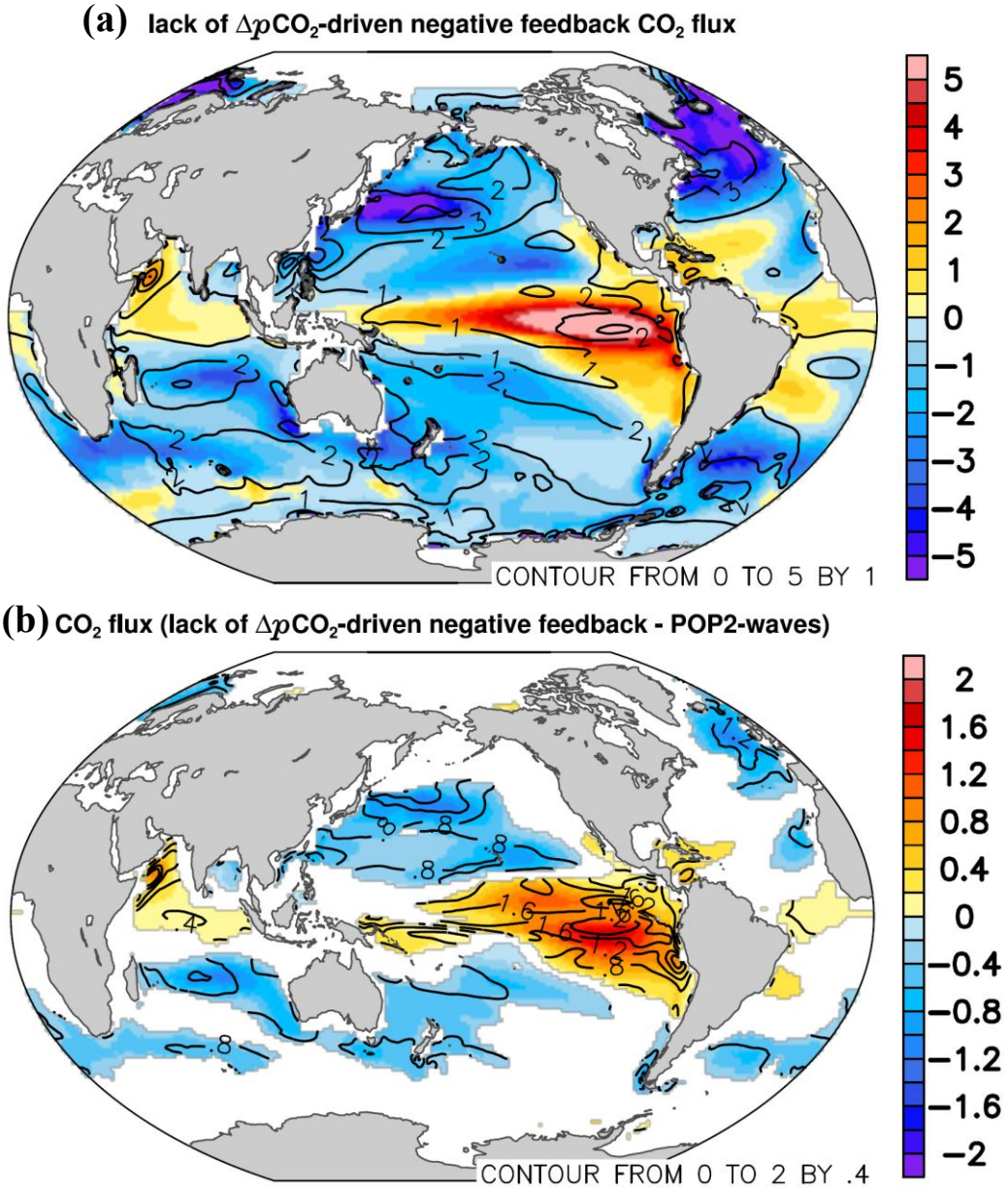

1492

1493 **Figure 10.** Estimated air–sea CO_2 flux assuming the absence of the ΔpCO_2-driven
1494 negative feedback mechanism. (a) Air–sea CO_2 flux calculated using uncoupled,
1495 independent ΔpCO_2 values from the B–CTL baseline and wave-dependent $k_{w,660}$
1496 formulations (labeled as the "lack of ΔpCO_2-driven negative feedback" case).
1497 Shading represents the climatological mean, and contours indicate the corresponding
1498 standard deviation (SD). (b) Spatial difference in CO_2 flux between the decoupled
1499 feedback case and the fully coupled POP2–waves simulation (decoupled minus
1500 POP2–waves). Shading denotes the mean difference, and overlaid contours indicate
1501 regions where the difference is statistically significant at the 95% confidence level
1502 based on a Student's t-test.

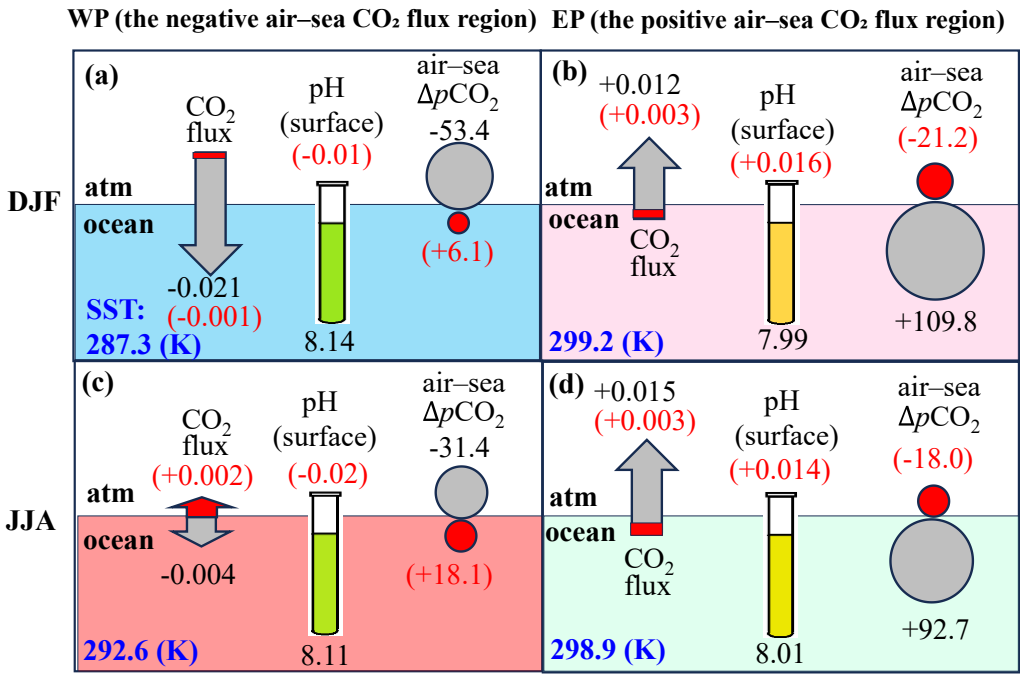

Figure 11. Schematic diagrams illustrate B–CTL (gray colors) and the differences between POP2–waves and B–CTL (red colors) in air–sea CO_2 flux (arrows), surface pH (tube colors indicator), and air–sea ΔpCO_2 (circle markers) over the oceanic CO_2 uptake region (WP; 160–180°E, 35–40°N) and the oceanic CO_2 outgassing region (EP; 230–250°E, 0–5°S). Each panel includes an ocean-atmosphere interface, with ocean color shading representing relative SST levels across different seasons. The lower-left corner displays the SST value, (a) WP in DJF seasonal mean, (b) EP in DJF seasonal mean, (c) WP in JJA seasonal mean, and (d) EP in JJA seasonal mean.